

830 H-15  
AUG 11 1978

NAS 1.60:1258

NASA Technical Paper 1258

COMPLETED  
ORIGINAL

# Low-Frequency Fluctuation Spectra and Associated Particle Transport in the NASA Lewis Bumpy-Torus Plasma

Chandra M. Singh, Walter M. Krawczonek,  
J. Reece Roth, Jae Y. Hong, Young C. Kim,  
and Edward J. Powers

AUGUST 1978

**NASA**

**NASA Technical Paper 1258**

# **Low-Frequency Fluctuation Spectra and Associated Particle Transport in the NASA Lewis Bumpy-Torus Plasma**

**Chandra M. Singh, Walter M. Krawczonek,  
and J. Reece Roth**  
*Lewis Research Center  
Cleveland, Ohio*

**Jae Y. Hong, Young C. Kim, and Edward J. Powers**  
*University of Texas  
Austin, Texas*



National Aeronautics  
and Space Administration

**Scientific and Technical  
Information Office**

1978

# LOW-FREQUENCY FLUCTUATION SPECTRA AND ASSOCIATED PARTICLE TRANSPORT IN THE NASA LEWIS BUMPY-TORUS PLASMA

by Chandra M. Singh,\* Walter M. Krawczonek, J. Reece Roth, Jae Y. Hong,<sup>†</sup>  
Young C. Kim,<sup>‡</sup> and Edward J. Powers<sup>‡</sup>

Lewis Research Center

## SUMMARY

The NASA Lewis bumpy-torus experiment employs a modified Penning discharge to produce and heat a plasma in a bumpy toroidal magnetic field. The strong radial electric field associated with the Penning discharge and the strong toroidal magnetic field give rise to a diversity of E/B phenomena, such as rotating waves and spokes, which in turn manifest themselves as space-time fluctuations of the plasma density and potential. The ultimate objective of the work reported herein is to further understand the nature and origin of the fluctuations and their connection with fluctuation-induced transport. The approach is to monitor the density and potential fluctuations; to digitize the data; and to generate, with the aid of a computer, various spectral properties by means of the fast Fourier transform. Of particular interest is the computer-generated transport spectrum that indicates in a quantitative way which fluctuation spectral components contribute to transport and which do not. All experimental measurements of the spectral characteristics of the plasma are given in absolute units rather than relative values. Preliminary measurements of the transport spectrum of the ion population are given, and it is shown that the fluctuation-induced transport is in order-of-magnitude agreement with that inferred from the steady-state current flowing to the electrodes that generate the plasma.

---

\*National Research Council - National Aeronautics and Space Administration Research Associate.

<sup>†</sup>University of Texas, Austin, Texas.

<sup>‡</sup>Professor of Electrical Engineering, University of Texas, Austin, Texas.

## INTRODUCTION

The NASA Lewis bumpy-torus facility is a steady-state plasma confinement device in which a toroidal plasma is acted upon by strong electric fields externally imposed along the minor radius of the plasma. It employs a modified Penning discharge to produce and heat a plasma in a bumpy toroidal magnetic field geometry produced by 12 superconducting coils, each having an inside diameter of 19 centimeters and being capable of producing 3 teslas on axis. The coils form a toroidal array 1.52 meters in major diameter. Figure 1 is an isometric cutaway drawing of the facility, details of which are given in reference 1. A Penning discharge occurs when circular electrode rings are placed at the midplane of one or more of the 12 toroidal sectors. The electrode rings can be biased with positive or negative potentials in excess of 10 kilovolts with respect to the grounded magnet dewars. All data reported herein were taken with positive electrode polarity. This combination of strong, crossed electric and magnetic fields can produce a steady-state deuterium plasma of density  $10^8$  to  $10^{12}$  particles per cubic centimeter, ion kinetic temperatures of 340 to 2500 electron volts, and electron kinetic temperatures of 8 to 140 electron volts. To avoid damage to the probes, we had to restrict

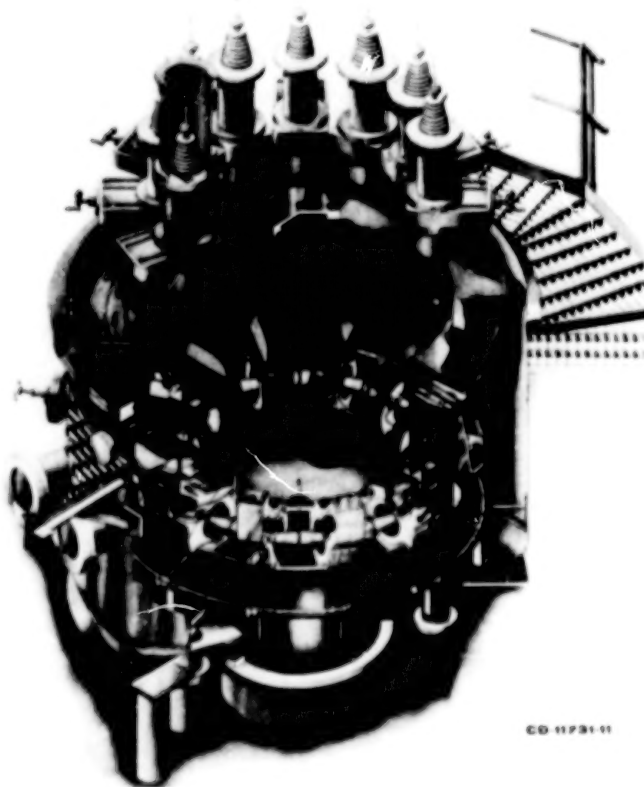


Figure 1. - Isometric cutaway drawing of NASA Lewis bumpy torus.



the operating conditions to the low ends of these ranges. The plasma in this investigation was subject to a steady-state radial electric field that ranged between 50 and 200 volts per centimeter. The results of investigations into other aspects of this plasma are reported in references 2 to 7.

The bumpy-torus plasma operates in two modes (refs. 2 and 3): the low-pressure mode (LPM), and the high-pressure mode (HPM). The low-pressure mode is characterized, in deuterium, by an electron temperature  $T_e$  greater than 35 electron volts and a neutral background density  $n_0$  below  $9 \times 10^{11}$  particles per cubic centimeter ( $2.7 \times 10^{-5}$  torr). The high-pressure mode has  $T_e$  less than 35 electron volts and  $n_0$  that usually are above  $9 \times 10^{11}$  particles per cubic centimeter ( $2.7 \times 10^{-5}$  torr).

When a positive voltage is applied to the midplane electrodes, the plasma floats at a positive potential approaching that of the midplane electrode rings. The presence of a high positive bias on the toroidal plasma leads to a radially outward electric field between the plasma and the grounded magnet dewars and vacuum chamber walls. A radially inward electric field exists between the anode rings and the plasma. The directions of the steady-state electric and magnetic fields acting on the plasma are shown in a schematic of the bumpy-torus plasma in figure 2. The plasma can thus support two oppositely directed E/B drift motions. The boundary of the plasma is defined by the inside diameter of the circular electrode rings. The plasma follows the magnetic field

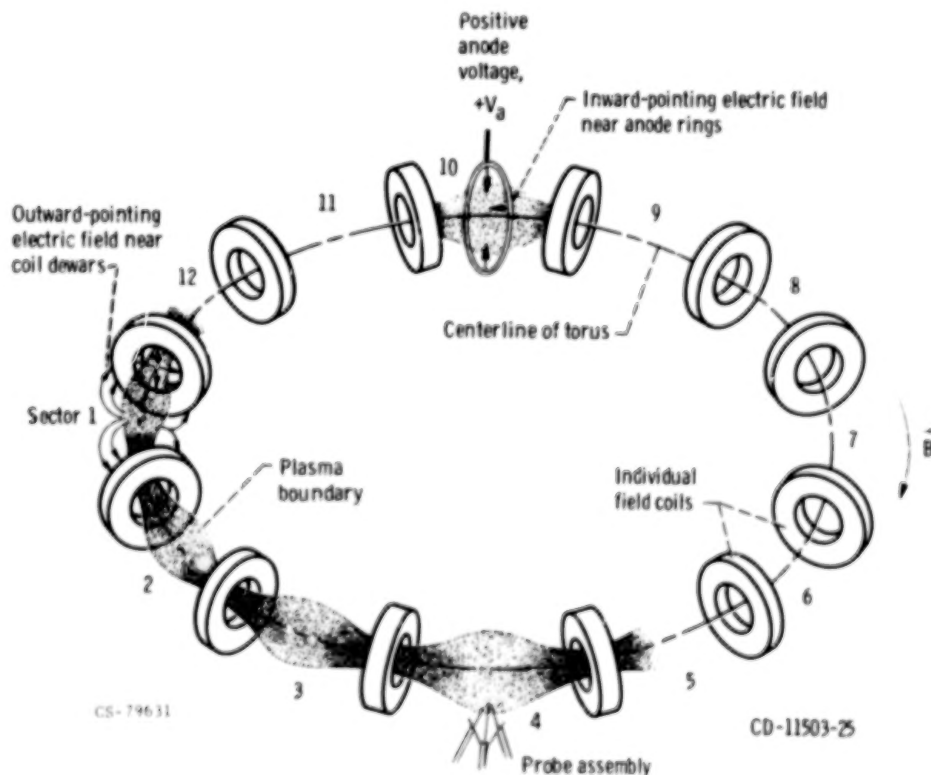


Figure 2 - Schematic drawing of bumpy-torus plasma with positive electrode polarity.

lines and narrows down as it passes through the throats of the magnetic field coils. Figure 3 shows the plasma in the equatorial plane of the torus.

The reservoir of free energy stored in the E/B drift motion of the toroidal plasma is a potential source of instabilities, fluctuations, and turbulence. Such disturbances can also be driven by the strong radial electric fields. The physics of crossed-field devices is reviewed in references 8 to 10. The fluctuations in density and potential have been implicated in the thermalization of the directed energy of the plasma particles and also in the transport of particles to the electrodes (refs. 2 and 11 to 15).

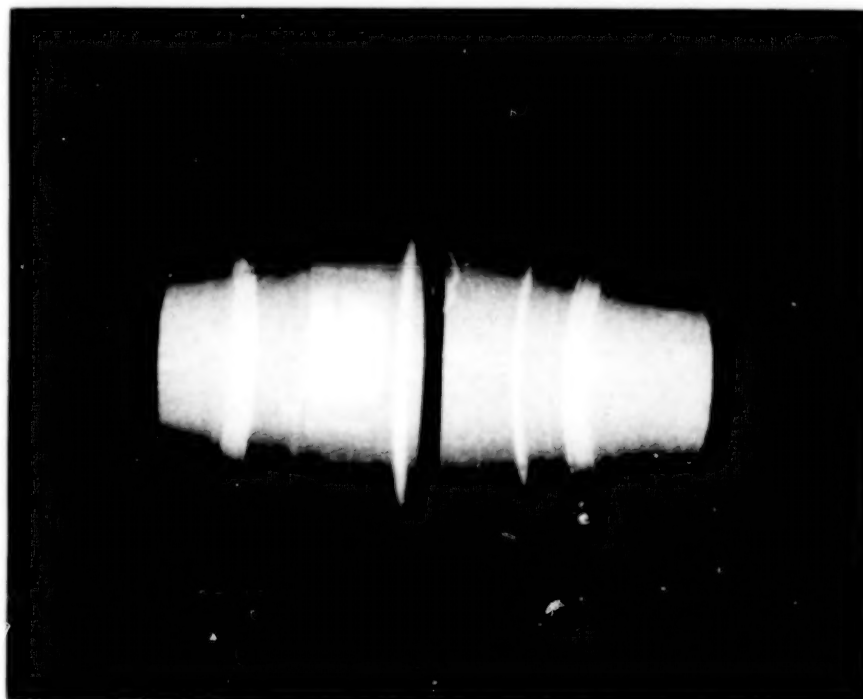


Figure 3. - Bumpy-torus plasma, viewed in equatorial plane of torus.

Plasma transport in fusion-oriented, crossed-field devices like the NASA Lewis bumpy torus is complicated by the presence of large steady-state electric fields, up to several kilovolts per centimeter (ref. 3). Another factor that makes the study of plasma transport interesting in this device is that  $T_i \gg T_e$ . (Symbols are defined in the appendix.) When  $T_i \gg T_e$ , space-charge sheath formation near the electrodes is not expected to be governed by the Bohm criterion (ref. 16). In addition, the current flow to the electrodes surrounding the plasma is not ambipolar (ref. 4): Only electrons flow to the anodes and only ions to the cathodes. This factor, along with the large, radial electric fields and the nonneutral nature of the sheaths, may affect the stability and transport of the plasma. A study of the density and the potential fluctuation spectra may reveal which portions of the spectrum cause transport and which are associated with

thermalization of the directed energy of the plasma. Knowing the dependence (refs. 17 and 18) of the current collected by the electrodes on plasma parameters and comparing this dependence with the fluctuation-induced transport should indicate whether or not fluctuations are the dominant transport mechanism.

The study of fluctuation-induced transport follows a digital approach: Density and potential fluctuations are monitored with the aid of probes, and the corresponding signals are digitized and stored in a computer where they are analyzed by fast-Fourier-transform (FFT) spectral analysis techniques. In particular, the amplitude, frequency, and wave numbers of the waves are determined from the computer-generated autopower and cross-power spectra. The FFT techniques are also used to generate the transport spectrum that quantitatively indicates which portions of the spectrum are contributing to the transport and which are not. This report deals with the low-frequency  $\omega \ll \omega_{ci}$  fluctuation spectrum and the associated fluctuation-induced radial particle transport in the NASA Lewis bumpy torus. The high-frequency emission spectrum of this plasma has been reported in reference 6. Different combinations of circular electrode rings of 18-centimeter inside diameter were placed at the midplane of the toroidal sectors. The numbering of the electrodes and the toroidal sectors is shown in figure 2. The fluctuation spectra and transport have been examined for a limited range of the neutral background density and voltage applied to the electrodes. It is important to realize that this diagnostic method will not necessarily measure diffusive transport resulting from binary collisions. It does, however, measure the transport resulting from fluctuating electric fields, which dominate in this plasma.

## FLUCTUATION DIAGNOSTICS AND DATA HANDLING

The day-to-day operation of the NASA Lewis bumpy-torus experiment requires the acquisition of analog and digital signals of various amplitudes and time durations. The neutral background density, magnetic field strength, electrode voltage and current, and background neutral gas impurities are routinely monitored (the last by mass spectrometer). When required by the experimental program, measurements can be made of X-ray and neutron production, ion kinetic temperature (by a neutral particle analyzer), time- and space-averaged electron density (by a polarization diplexing microwave interferometer), and 10-megahertz to 1.2-gigahertz electromagnetic emission (by a miniature, rf, coaxial probe).

### Data Acquisition

This investigation uses a set of capacitive and Langmuir probes to measure the potential and density fluctuations, respectively, in the frequency range from 1 kilohertz

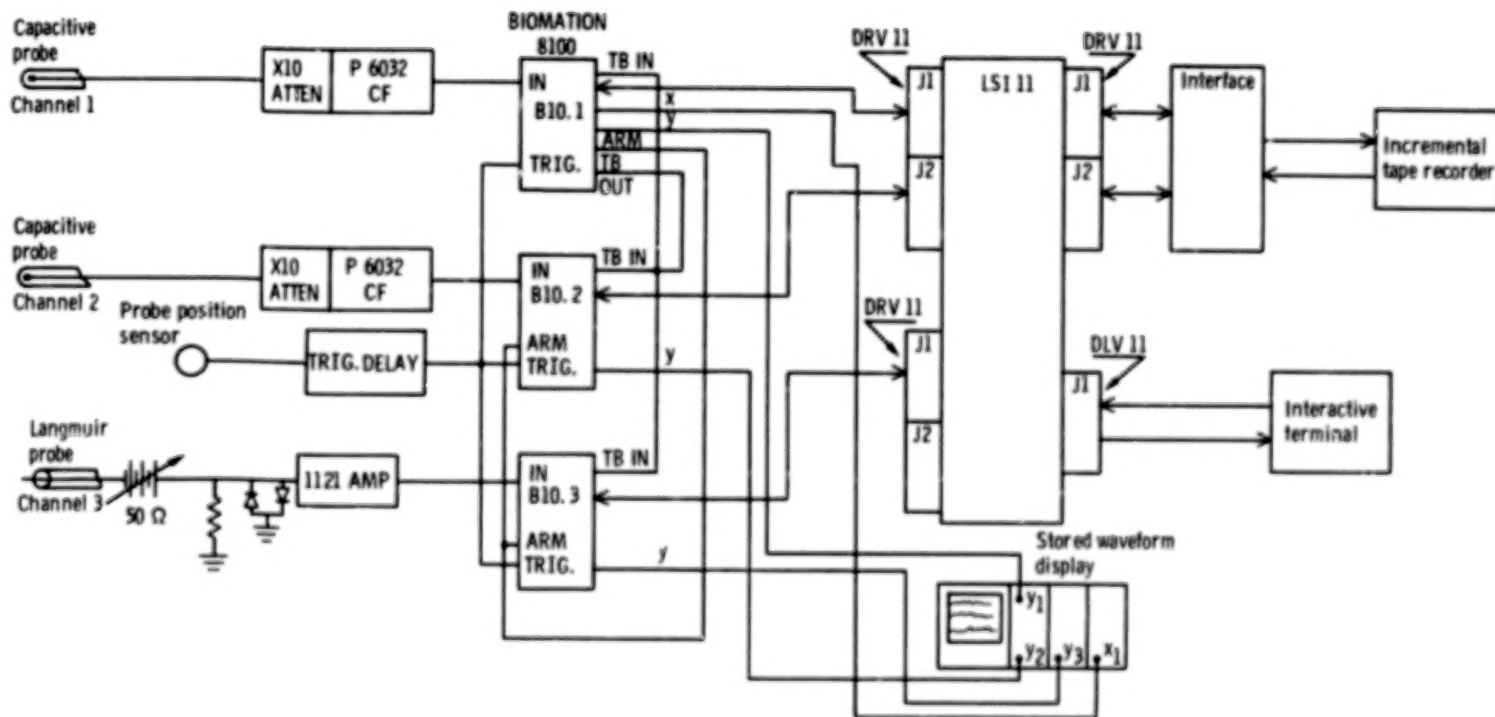


Figure 4. - Block diagram of data-acquisition system for measuring radial particle transport.

to 5 megahertz. Figure 4 is a block diagram of the data-acquisition system. The probes were hydraulically actuated into the plasma for short times to take data. The upper limit on probe dwell time was the point at which the probe tips became red hot. The maximum dwell time with this actuation system was 0.7 second. Inserting the probe assembly into the plasma caused a change of less than 5 percent in the current drawn by the electrodes. We therefore assume that the gross plasma characteristics do not change significantly during the time the probes are in the plasma.

The travel of the probe assembly was so adjusted that the capacitive probe in channel 1 was located 3 millimeters inside the boundary defined by the inner circumference of the electrodes in adjacent sectors of the torus, or 7 centimeters from the plasma axis in the equatorial plane. The capacitive probe in channel 2 was  $30^\circ$  above the equatorial plane, in the same vertical plane and at the same plasma radius as the Langmuir probe in channel 3. The Langmuir probe in channel 3 was in the equatorial plane at the same plasma radius of 7 centimeters. However, the capacitive probe in channel 1 and the Langmuir probe were displaced axially 1 centimeter from each other. Figure 5 is a closeup view of the probes in the probe mount. With this probe arrangement (i. e., channels 1 and 3) the potential and density fluctuations can be measured at the same



Figure 5. - Closeup view of probes in probe mount.

minor radius in the plasma, without reference to the axial dimension for waves whose axial wavelength  $\lambda_{\parallel}$  is much larger than 1 centimeter. With the capacitive probes in channels 1 and 2 the azimuthal wave number  $k_{\theta}$  of the potential fluctuations can be measured. The probe assembly is near the midplane of sector 4, as shown in figure 2. The microwave interferometer is in sector 10. The axial and radial wave numbers  $k_{\parallel}$  and  $k_r$  have not been measured in this study. Figure 6 shows the probe assembly and its hydraulic actuating system, and figure 7 shows this assembly mounted on the vacuum tank.

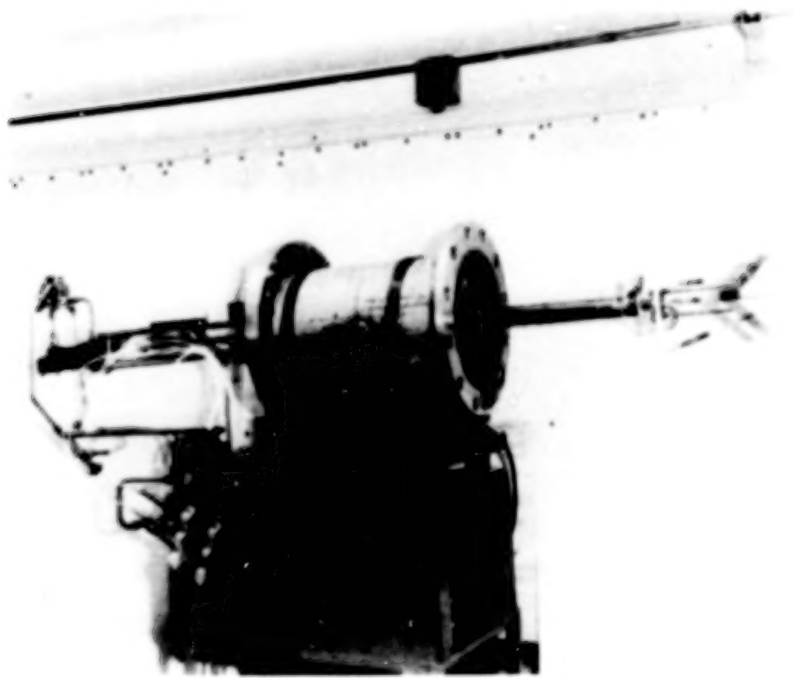


Figure 6. - Probe actuator assembly.

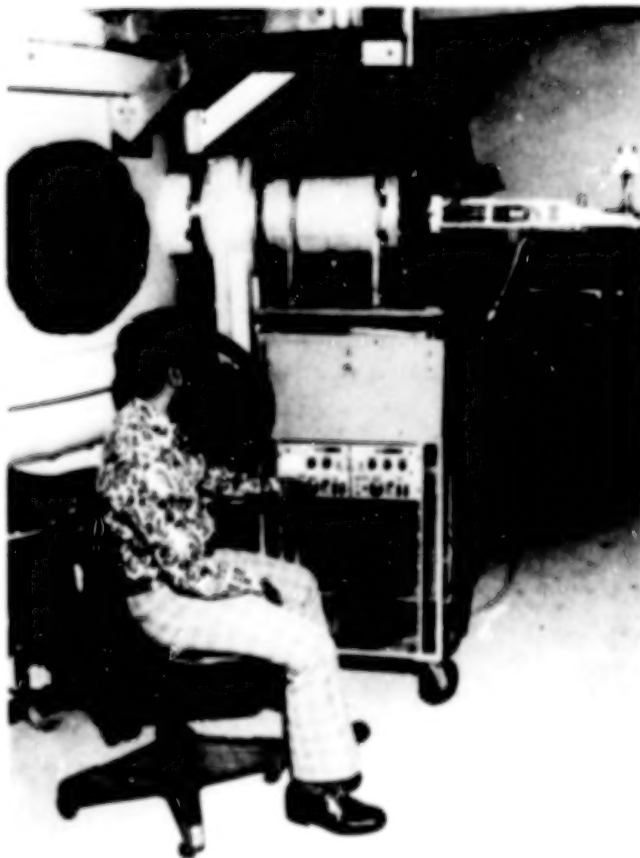


Figure 7. - Probe actuator assembly on vacuum tank

## Data Processing and Analysis

The data-processing system consists of waveform recorders, a magnetic tape recorder, a microcomputer, and a computer terminal (fig. 8). In a typical experimental run, the probes were actuated into the plasma; the data were recorded on the waveform recorders; the probes were brought out of the plasma; and finally, after the sampled waveforms were inspected for signal saturation or other defects in the data, the data were recorded on magnetic tape. The tape was then sent to the University of Texas at Austin for processing.

Fast-Fourier-transform (FFT) spectral analysis techniques were used to generate autopower and cross-amplitude spectra from which the amplitude, frequency, and wave number of each wave in the fluctuation spectrum were determined. The transport spectrum was also computed to provide quantitative insight into how much transport is associated with the various spectral bands. The raw waveform data were also used to generate such amplitude statistics as the probability density functions, the mean, the standard deviation, the skewness, the kurtosis, and higher moments of the distribution

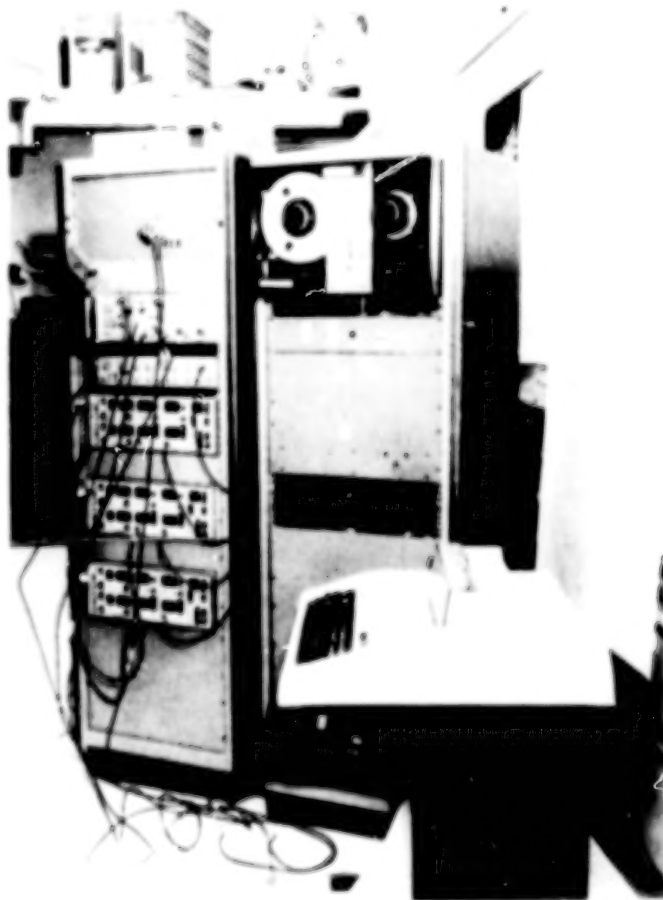


Figure 8. - Data-acquisition system.



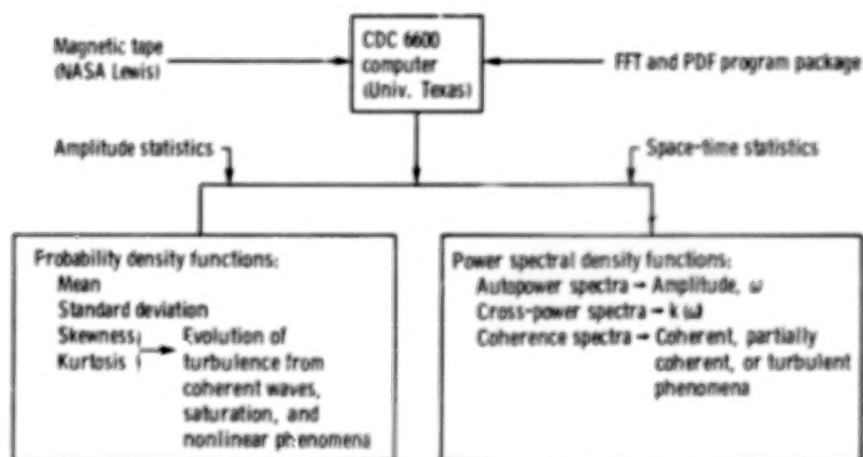


Figure 9. - Schematic of data-processing system.

function. The various data-processing functions performed on the taped data at the University of Texas are shown on the block diagram in figure 9.

### System Calibration

Before the plasma data were processed and analyzed, the data-acquisition system was checked by known test waveforms from a signal generator. Waveforms of known amplitudes, frequency, and waveshape were applied to the input of all three waveform recorders. We concluded, after generating power spectra for different waveforms, frequencies, and sampling intervals, that there was no measurable instrument-related phase shift (time delay) in the data from the three channels. Further details on the calibration procedure and specific examples of test waveform spectra are given in reference 5. The constant phase shift between channels discussed in reference 5 has, however, been eliminated in the present series of runs.

Capacitive probes. - Capacitive probes were used to measure the low-frequency ( $\omega \ll \omega_{ci}$ ) electrostatic potential fluctuations. It is shown in reference 19 that a capacitive probe has a better frequency response than a high-impedance, floating Langmuir probe. The attenuation and frequency response of each capacitive probe were measured: The frequency response was flat from 1 kilohertz to 5 megahertz. From the probe's attenuation the absolute peak-to-peak amplitude of the potential fluctuations in the plasma could be determined.

Langmuir probe. - The simplicity and ease of operation of a Langmuir probe make it a widely used diagnostic tool for the measurement of spatially resolved plasma density. However, the theory of probe operation (ref. 20) in hot ( $T_i \gg T_e$ ), drifting plasmas with strong magnetic fields is not fully understood. Therefore, a microwave inter-



ferometer was used to obtain the absolute value of time- and space-averaged electron density. A single Langmuir probe was used to measure the steady-state floating potential and the density fluctuations. The Langmuir probe was connected to a 100-megohm input impedance probe to measure the dc floating potential.

From the instantaneous floating potential the amount of dc bias from a power supply that is required to measure the ion or electron saturation current can be determined. The electron temperature was in all cases much less than the energy corresponding to the bias potential. In all the runs reported herein, fluctuations in the ion saturation current were measured (ref. 16). A measurement of the electron saturation current caused the probe to draw large currents, making the probe tips glow red hot and the probe eventually destroy itself. All the data presented herein were taken with short enough dwell times to avoid any effects on the data (e.g., noise) due to incandescence of the probe or arcing to the probe tip.

The radial profile and waveform of the ion saturation current also yield information on the density profile and the density concentrations that reveal the presence or absence of rotating spokes. Electron spokes in high-vacuum magnetrons and other axisymmetric,

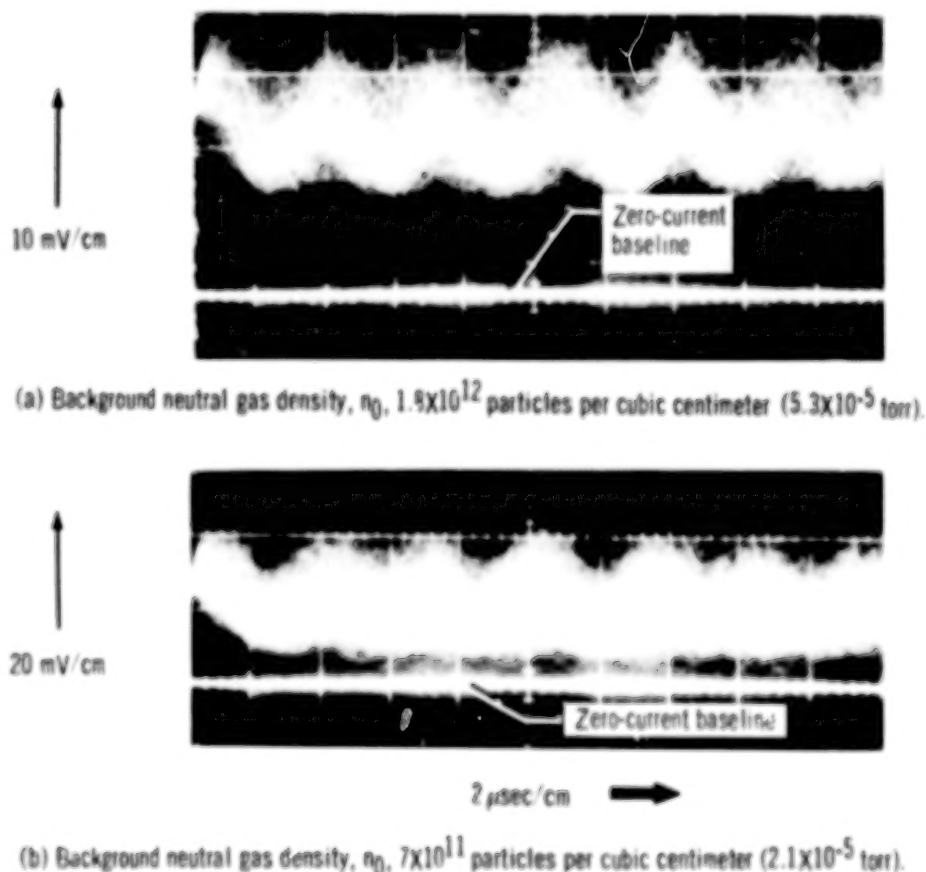


Figure 10. - Fluctuations in ion saturation current. Electrode 10 in place; anode voltage, 2 kilovolts.

crossed-field devices propagate azimuthally with electron density fluctuations  $\tilde{n}_e/\bar{n}_e \approx 1$ . The spoke usually occupies only a fraction of the minor circumference. In high-pressure, crossed-field discharges (ref. 9), the plasma forms one or more rotating spokes, but eventually ionization, diffusion, or shock formation can lead to a spread in the spoke azimuth until a continuous plasma disk results. Such cases are characterized by  $\tilde{n}_e/\bar{n}_e < 1.0$ .

Langmuir probe measurements of the ion saturation current in the NASA Lewis bumpy torus show that  $\tilde{n}_e/\bar{n}_e \leq 1.0$ . A representative case is shown in figure 10. The lower trace is the zero-current baseline; the upper trace shows the dc, coupled voltage drop across a 50-ohm resistor in the Langmuir probe circuit. The shape of the waveform is indicative of the shape of the density distribution inside the density perturbation.

### EXPERIMENTAL OPERATING CONDITIONS

This investigation was exploratory, and no attempt was made to obtain parametric variations of the plasma dispersion or transport characteristics. For this series of runs, the magnetic field was held constant at 2.4 tesla at the coil throats and 0.67 tesla at the Langmuir probe. The electrode polarity was positive, which imparts a positive potential to the entire plasma. This resulted in an outward-pointing electric field at the probe, since the probes were located at the plasma boundary, as shown in figure 2. Deuterium gas was used in all runs.

Approximately 30 individual experimental runs yielded valid data. The operating conditions of nine runs of particular interest are given in table I, including the number of electrode rings that were used to generate the plasma and the sectors in which the electrodes were located. The sector numbering convention is illustrated in figure 2. The probe assembly was in sector 4, diametrically opposite the sector containing the microwave interferometer. The positive voltages applied to the electrodes (column 5) can reach several tens of kilovolts, but had to be kept low during these investigations to avoid arcing to the Langmuir probe.

The electrode current in table I (column 6) is the total ion current flowing from the plasma to the power supply, and the background neutral deuterium gas density (column 7) was corrected for the appropriate gage factor. The electron number density (column 8) was measured with the polarization diplexing microwave interferometer (ref. 4), and the relative density fluctuation (column 9) is the ratio of one-half the peak-to-peak amplitude to the mean value, as measured on oscilloscope traces. The density fluctuations were measured by connecting the Langmuir probe to ground through a 50-ohm resistor. Since the plasma was floating at high positive potentials during these runs, the ion saturation current could be obtained without additional bias voltage.

TABLE I - OPERATING CONDITIONS

Run	Figure	Number of electrodes	Sectors containing electrodes	Anode voltage, $V_a$ , kV	Anode current, $I_a$ , A	Background neutral gas density, $n_0$ , $\frac{\text{particles}}{\text{cm}^3}$	Average electron number density, $\bar{n}_e$ , $\frac{\text{electrons}}{\text{m}^3}$	Relative density fluctuation, $\delta n_e / \bar{n}_e$	Mode of operation <sup>a</sup>
1	21, 22	11	Not 4	2	0.12	$7.0 \times 10^{11}$	$1.7 \times 10^{15}$	0.50	LPM
2	11, 20	11	Not 4	1	.026	7.0	.46	.20	LPM
3	12, 17, 25	2	1, 7	1	.12	7.0	2.5	.52	LPM
4	18	11	Not 4	1	.024	18.0	.50	.40	HPM
5	15	2	5, 6	2	.19	3.6	2.0	.48	LPM
6	27, 28	1	10	1	.12	18.0	6.2	.60	HPM
7	16	1	10	1	.11	7.0	4.1	1.0	LPM
8	14, 19, 26	2	1, 7	1.2	.21	16.0	5.3	.19	HPM
9	13, 24	2	3, 9	1	.082	7.0	2.9	.67	LPM

<sup>a</sup>LPM denotes low-pressure mode; HPM denotes high-pressure mode.

## CHARACTERISTICS OF AMPLITUDE DISTRIBUTION FUNCTION

### Theoretical Considerations

The first step in analyzing the plasma fluctuation data was to determine the properties of their amplitude distribution functions. In digitizing the analog signals, the waveform recorders sampled 2048 equally spaced points along the waveform and at each point could distinguish an 8-bit amplitude range, or 256 increments of signal amplitude. These 256 increments were assigned to one of 60 amplitude cells. The computer program places each of the 2048 waveform samples into an appropriate cell. The results, divided by the total number of samples, is the amplitude probability function, examples of which are given here. The computer program determines the mean value of the fluctuation amplitudes and shifts the zero of amplitude to the nearest amplitude cell for plotting. The  $p^{\text{th}}$  moment of  $f(x)$  is defined as

$$\sigma(p) \equiv \frac{\int_{-\infty}^{\infty} x^p f(x) dx}{\left[ \int_{-\infty}^{\infty} x^2 f(x) dx \right]^{p/2}} \quad (1)$$

where the mean value of the variable  $x$  is zero. The computer program calculates moments up to  $p = 7$ . The moments for some common probability density functions and for some common waveforms are given in table II. The standard deviation  $\sigma(2)$  is a measure of the width of the distribution function, or the degree of spread about the mean value. The skewness  $\sigma(3)$  is a measure of the asymmetry of the distribution function. Negative values of skewness imply distribution functions that are lopsided to the right of the mean value; positive values imply the opposite. The kurtosis  $\sigma(4)$  is a measure of how much time the signal spends in the wings of the distribution: A kurtosis of 1.0

TABLE II. - MOMENTS FOR SOME COMMON PROBABILITY  
DENSITY FUNCTIONS AND WAVEFORMS

Moment, $p$	Square wave of peak am- plitude $A$	Sinusoid of peak ampli- tude $A$	Full-wave rectified sine wave of peak amplitude $A$	Gaussian random noise
	Moment			
1 - Mean	0	0	0.637 $A$	0
2 - Standard deviation	$A$	0.707 $A$	0.308 $A$	$\sigma$
3 - Skewness	0	0	-0.497	0
4 - Kurtosis	1.0	1.5	1.93	3
5 - Superskewness	0	0	-2.11	0
6 - Superkurtosis	1.0	2.5	5.07	15
7 - Hyperskewness	0	0	-7.69	0
8 - Hyperkurtosis	1.0	4.375	15.8	105

implies that the signal spends all its time at the extreme values of the range (in the manner of a square wave); higher positive values imply increasingly centralized, delta-function-like distributions. The higher moments, above  $p = 4$ , do not appear to add new physical content to the lower moments, and therefore will not be considered further herein. The moments for a square wave, for a sinusoid, for a full-wave rectified sine wave, and for Gaussian random noise are shown as examples in table II.

The moments of the probability distributions for the runs listed in table I are given in table III. The standard deviation is given directly in volts and is (the first entry in table III) as large as 45 percent of the electrode voltage. Most deviations range from 10 to 30 percent of the electrode voltage. These very violent potential fluctuations must be expected to play a role in the stability and transport of the plasma. The kurtosis of nearly all runs is close to 3.0, which is characteristic of Gaussian random noise, for both potential and density fluctuations. An exception is the first run, in which the kurtosis is close to that of a sinusoid. As shown later, this run is char-

TABLE III. - MOMENTS OF PROBABILITY DISTRIBUTIONS

Run	Figure	Capacitive-probe potential fluctuations						Langmuir-probe density fluctuations (channel 3)		
		Near Langmuir probe (channel 1)			30° above Langmuir probe (channel 2)			Standard deviation, $\sigma$	Skewness	Kurtosis
		Standard deviation, $\sigma$	Skewness	Kurtosis	Standard deviation, $\sigma$	Skewness	Kurtosis			
1	---	780	-0.12	1.6	900	-0.08	1.6	3.2	-0.16	2.3
2	11	270	-.47	2.2	300	-.49	2.2	1.2	-.03	3.7
3	12	110	-.53	3.4	160	.02	2.8	2.7	.21	3.2
4	---	100	-.52	3.2	110	-.53	3.3	.21	.22	3.1
5	---	210	.27	2.8	230	.55	3.7	4.1	.55	3.9
6	---	62	-.04	3.0	110	.11	2.6	8.5	.72	3.1
7	---	99	-.11	2.7	120	-.01	2.7	16	.97	4.0
8	14	95	-.18	3.0	81	-.43	3.5	2.1	.24	3.2
9	15	110	-.25	2.4	140	-.21	2.5	5.2	.94	4.4

acterized by an extremely coherent rotating spoke at a single frequency. For the approximately 30 experimental runs analyzed, the skewness of the density fluctuation distribution (channel 3 in table III) seems to assume high positive values, but that of the potential fluctuations tends to be smaller and to depend on the circumstances of the run.

#### Low-Pressure Mode

Some examples of the distribution functions listed in table III are given for the low-pressure mode of operation. Figure 11 gives the distribution functions for the second run in tables I and III. Each point plotted represents the fraction of the 2048 sample points in the cell that corresponds to the potential or density amplitude plotted on the abscissa. This run illustrates a condition in which the potential distribution is moderately highly skewed, as a result of the raw potential waveform being cycloidal with the cusps pointing downward. The density distribution function is nearly symmetric. Figure 12 gives the distribution functions for the third run in tables I and III. This run illustrates a condition for which the kurtosis of all the distributions is close to that of Gaussian random noise but for which the skewness of the two potential distributions differs substantially. Finally, figure 13 gives the distribution functions for the ninth run in tables I and III. This run illustrates a distribution for which the density fluctuations are highly skewed but the potential fluctuations much less so.

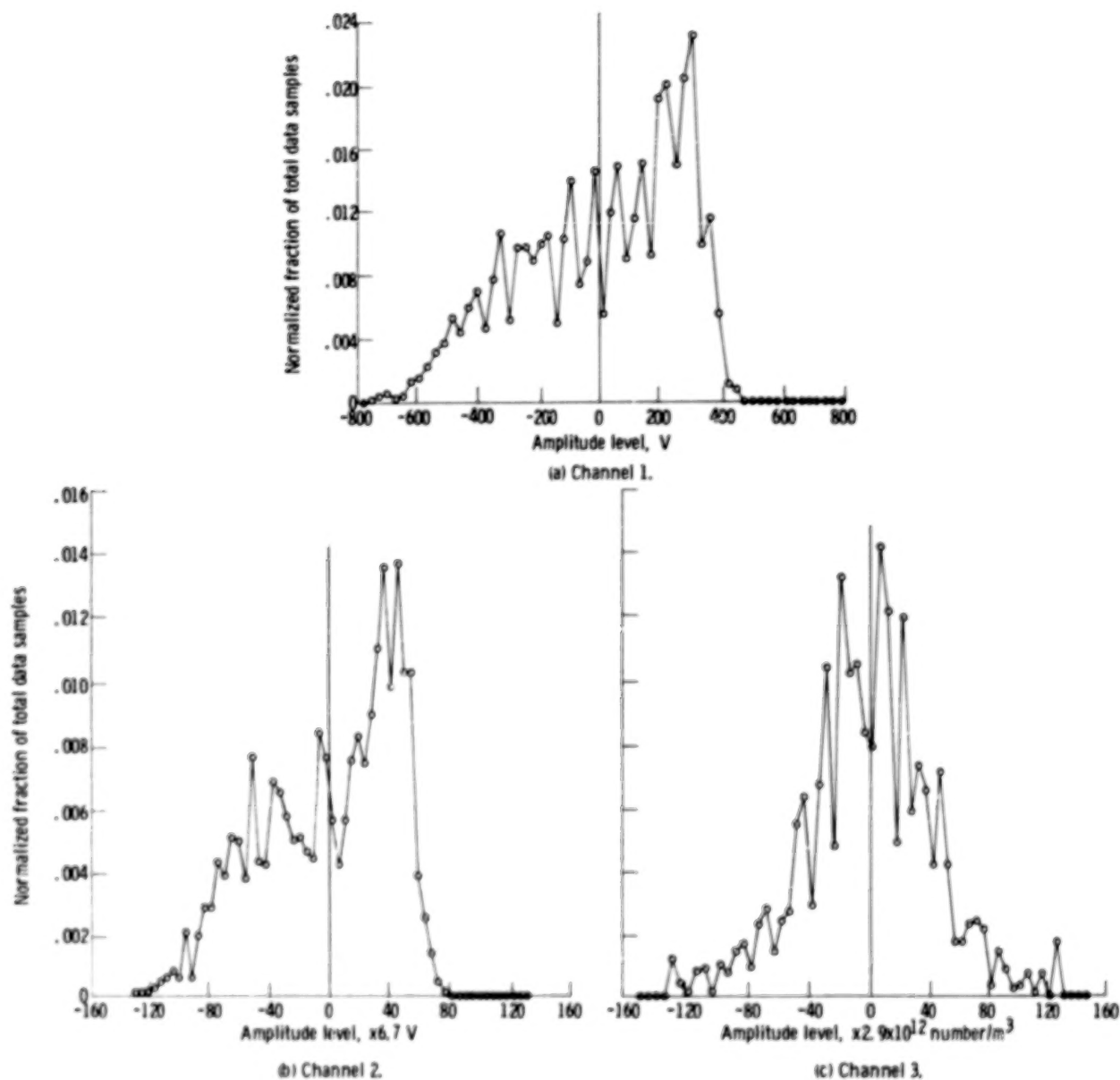
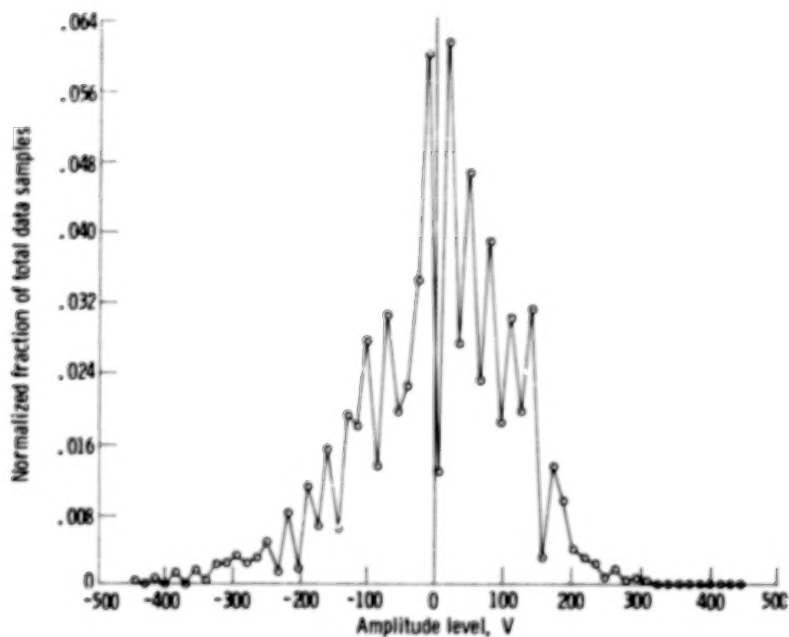
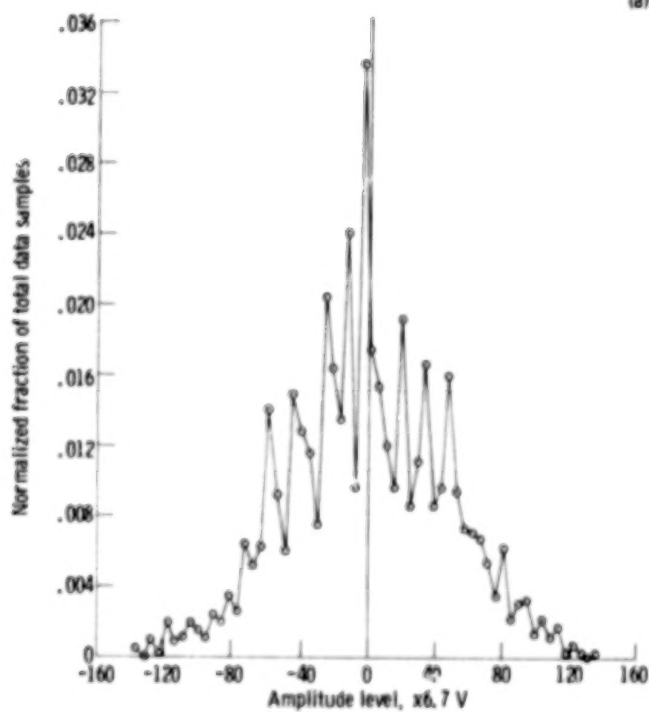


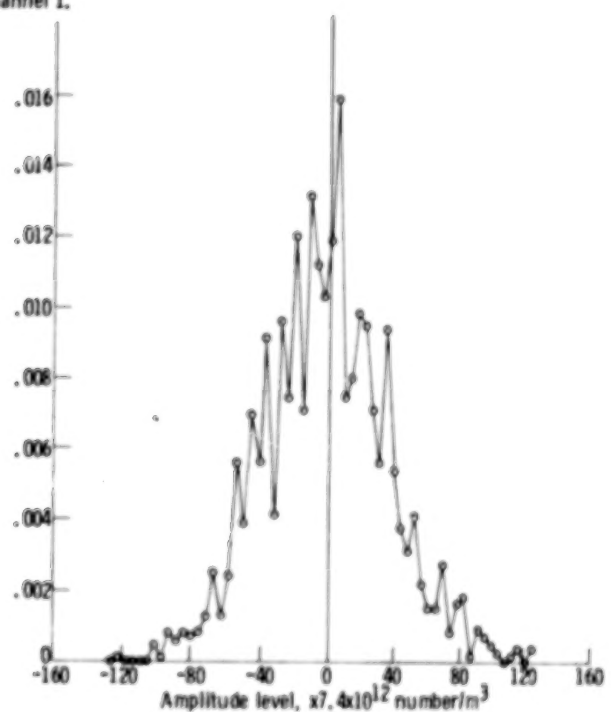
Figure 11. - Probability density functions for run 2 of table I.



(a) Channel 1.



(b) Channel 2.



(c) Channel 3.

Figure 12. - Probability density functions for run 3 of table I.



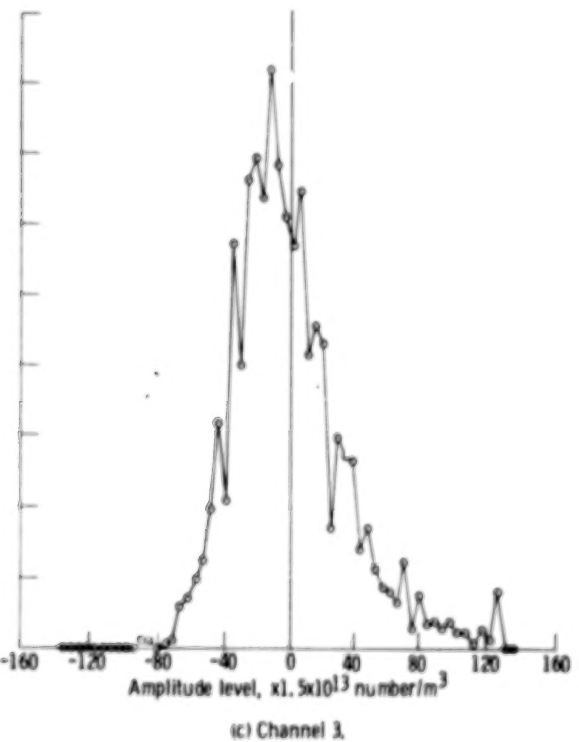
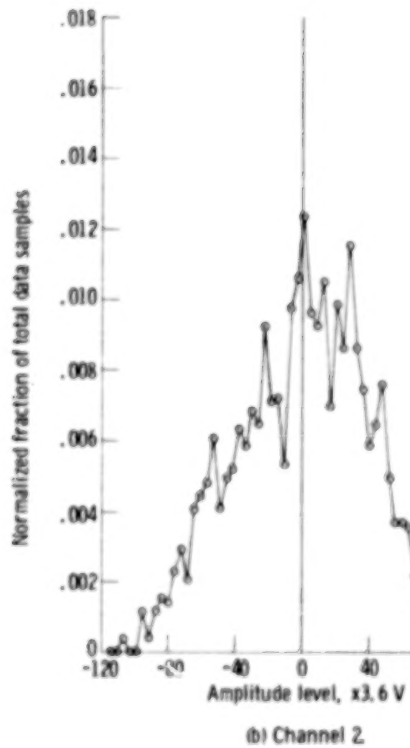
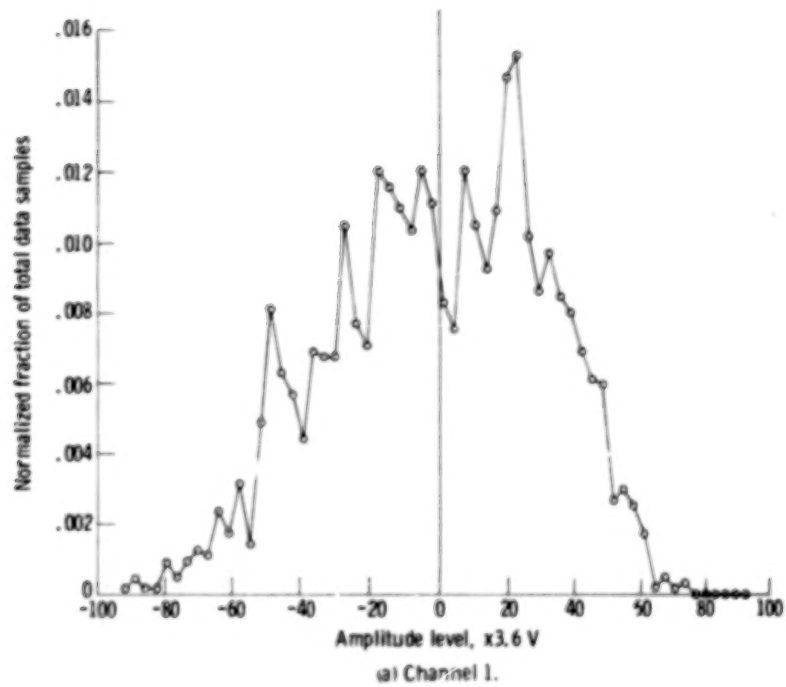


Figure 13. - Probability density function for run 9 of table 1.



## High-Pressure Mode

A characteristic example of the amplitude probability distribution function for the high-pressure mode (HPM) of operation (eighth entry in table III) is given in figure 14. The distribution functions of the density and potential fluctuations tend to have a kurtosis near 3.0, which is characteristic of Gaussian random noise, but they also have nonzero values of skewness with the potential distributions being negative and

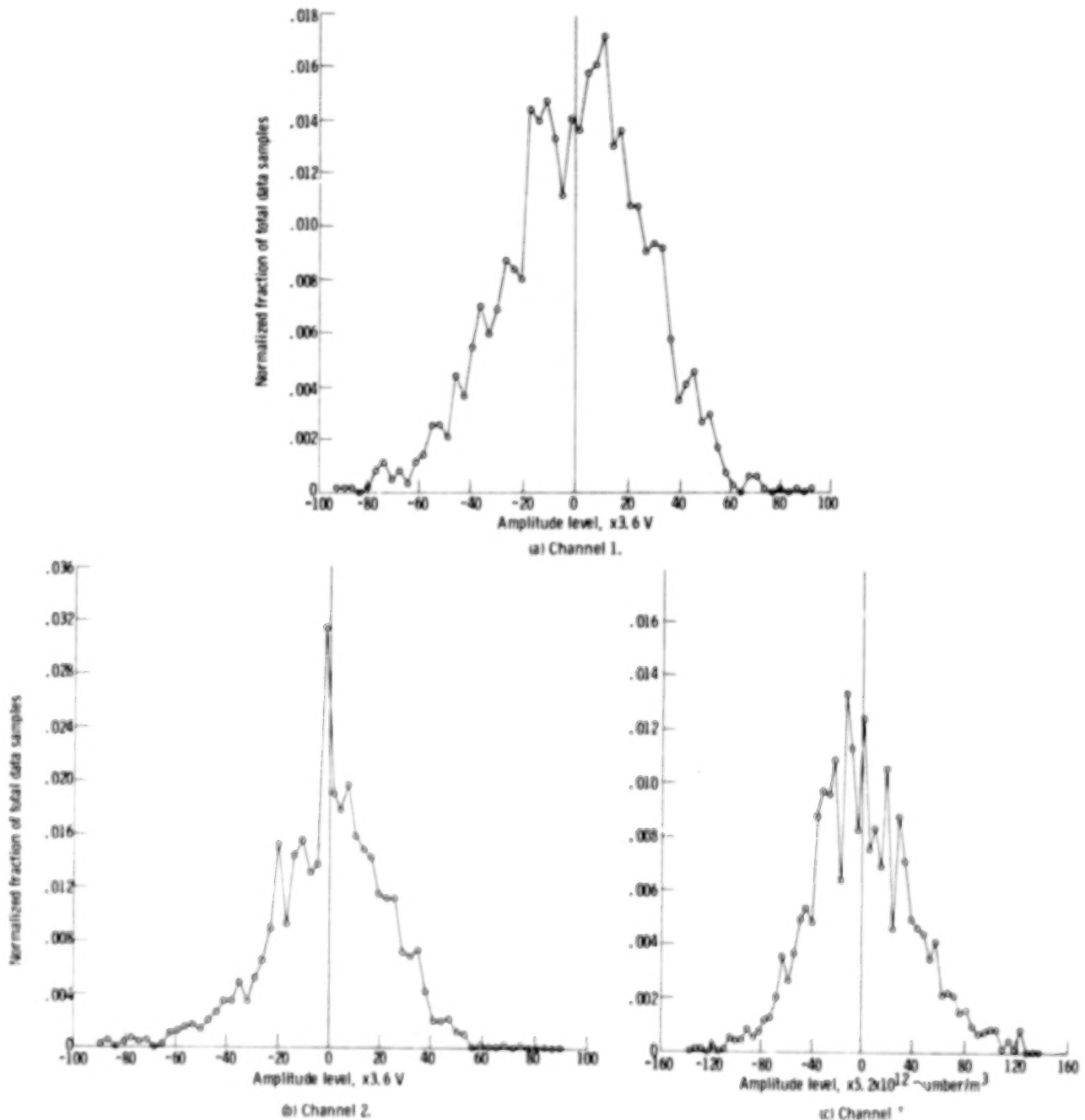


Figure 14. - Probability density function for run 8 of table 1.

skewed to the right and density distributions being positive and skewed to the left. The tendency of both modes of operation to have nonzero values of skewness can be understood as a result of the cycloidal, cusplike waveforms associated with the motion of a rotating spoke as it moves past the probes (refs. 2 and 3). The tendency of the skewness to have opposite signs for the density and potential fluctuations can be understood if both waveforms are cusplike but point up or down in opposite directions.

## AZIMUTHAL DISPERSIVE CHARACTERISTICS OF PLASMA

### Theoretical Considerations

Low-frequency potential fluctuation spectra were obtained by processing the signals  $\tilde{\varphi}_1(t)$  and  $\tilde{\varphi}_2(t)$  from the two capacitive probes in channel 1 and channel 2, respectively. A schematic of the data-processing system is shown in figure 9. The computer output consists of plots of the autopower spectrum, the cross-power spectrum (both amplitude and phase), and the squared coherency spectrum between channels 1 and 2.

The underlying principles behind fast-Fourier-transform analysis of plasma fluctuation data are described in detail in references 5 and 21 to 23. Here we give a brief review of digital spectral analysis and how it may be used to analyze and interpret plasma fluctuation data. The approach is to take the two capacitive probe signals  $\tilde{\varphi}_1(t)$  and  $\tilde{\varphi}_2(t)$ , to digitize them, and to compute their respective Fourier transforms  $\Phi_1(\omega)$  and  $\Phi_2(\omega)$  by using the fast-Fourier-transform algorithm. The autopower spectrum<sup>1</sup> of channel 1 is given by  $P_{11}(\omega) = \Phi_1(\omega)\Phi_1^*(\omega)$ , where the asterisk denotes a complex conjugate. The autopower spectrum for channel 2 is computed in a similar way.

Of particular importance is the cross-power spectrum between  $\varphi_1(t)$  and  $\varphi_2(t)$  since it can suggest the presence of propagating waves. The cross-power spectrum is given by  $P_{12}(\omega) = \Phi_1(\omega)\Phi_2^*(\omega)$  and is a complex quantity. In this transport work, described later in this section, we considered the real and imaginary parts of the cross-power spectrum, which are known as the co- and quadrature spectra, respectively. However, in studying the properties of the fluctuations, it is convenient to express the cross-power spectrum in terms of an amplitude spectrum  $|P_{12}(\omega)|$  and a phase  $\theta_{12}(\omega)$  spectrum. From the definition of  $P_{12}(\omega) = \Phi_1(\omega)\Phi_2^*(\omega)$ , it is clear that the cross-amplitude spectrum is given by  $|P_{12}(\omega)| = |\Phi_1(\omega)| |\Phi_2(\omega)|$  and the phase spectrum by  $\theta_{12}(\omega) = \theta_1(\omega) - \theta_2(\omega)$ , where  $\theta_1(\omega)$  is the phase of  $\Phi_1(\omega)$  and  $\theta_2(\omega)$  is the phase of

---

<sup>1</sup>Strictly speaking, the autopower spectrum is defined as  $P_{11}(\omega) = \lim_{T \rightarrow \infty} \left\{ \frac{1}{T} E[\Phi_1(\omega)\Phi_1^*(\omega)] \right\}$ , where  $T$  is the time duration of the  $\tilde{\varphi}_1(t)$  waveform used to compute  $\Phi_1(\omega)$ . A similar definition applies to the cross-power spectra.

$\Phi_2(\omega)$ . We use the important fact that the phase spectrum preserves phase information in the form of a phase difference to determine the wave number of each wave in the measured fluctuation spectrum. For example, if a wave is present at frequency  $\omega$ , the phase shift that the wave undergoes in propagating from one probe to another will be given by  $\theta_{12}(\omega)$  and will be equal to  $k(\omega)\Delta s$ ; thus  $\theta_{12}(\omega) = k(\omega)\Delta s$ . This equation suggests then that  $k(\omega)$  can be determined by taking the computer-generated phase spectrum  $\theta_{12}(\omega)$  and dividing by  $\Delta s$ , the known distance of separation between the probes. In cylindrical geometry, and for probes displaced azimuthally by  $\Delta\theta$ ,  $\Delta s = R_p \Delta\theta$  and  $k_\theta = m(\omega)/R_p$ , where  $R_p$  is the radial position of the probes and  $m(\omega)$  is the azimuthal mode number of the wave. With this information it is easy to show that  $m(\omega) = \theta_{12}(\omega)/\Delta\theta$ .

To summarize, from the peaks in either the autopower spectrum or the cross-amplitude spectrum  $|P_{12}(\omega)|$  the amplitude and frequency can be determined for each of several waves in the fluctuation spectrum. From the phase spectrum  $\theta_{12}(\omega)$  the corresponding wave number  $k(\omega) = \theta_{12}(\omega)/\Delta s$  or azimuthal mode number  $m(\omega) = \theta_{12}(\omega)/\Delta\theta$  can be determined. Knowledge of the wave number permits computation of the phase velocity  $\omega/k$  at each frequency. The phase velocity can be written

$$v_{ph\theta} = \frac{\omega}{k_\theta(\omega)} = \frac{\omega R_p \Delta\theta}{\theta_{12}(\omega)} \quad (2)$$


and can be obtained from the computer-generated phase plots of  $\theta_{12}(\omega)$  versus  $\omega$ . From the magnitude, direction, and parametric variation of the phase velocity the wave can often be identified.

Another spectral quantity of some importance is the coherence spectrum, defined as  $|\gamma_{12}(\omega)| = |P_{12}(\omega)|/[P_{11}(\omega)P_{22}(\omega)]^{1/2}$ . Its properties are discussed in both references 23 and 24. Basically, it is a measure of the degree of mutual coherence between the signals  $\tilde{\varphi}_1(t)$  and  $\tilde{\varphi}_2(t)$ , with the difference in phases ignored. The coherence spectrum is bounded by zero (incoherent case) and unity (perfectly coherent fluctuations). Values between these two ideal limits correspond to a partially coherent case. In the following discussion, computer-generated plots of  $|\gamma_{12}(\omega)|^2$  are shown. High values of coherence are indicative of high signal-noise ratios, and conversely.

### Low-Pressure Mode

Some characteristics of the peaks in the autopower spectra of the experimental runs listed in table I are shown in table IV. Some had more than one peak in the spec-

TABLE IV. - CHARACTERISTICS OF TRANSPORT SPECTRAL PEAKS

Run	Figure	Peak frequency, kHz	Azimuthal phase velocity at peak, $v_{ph\theta}$ , cm/sec	Channel 1 autopower peak amplitude, V	Channel 2 autopower peak amplitude, V	Channel 3 autopower peak amplitude, $m^{-3}$	Peak transport rate, number/ $m^2 \cdot sec$	Total cumulative transport rate, number/ $m^2 \cdot sec$	Total current (calculated), A	Direction of radial transport	
1	21	20	$1.6 \times 10^6$	350	400	$1.2 \times 10^{14}$	$37 \times 10^{16}$	$15 \times 10^{17}$	0.53	Inward	
2	20	15	.61	190	210	.56	22	4.2	.15		
3	25	42	$\approx 0$	24	22	.49	$\approx 0$	.08	.003		
4	29	---	$\approx 0$	---	---	-----	-----	.027	.001		
5	---	30	2.9	57	65	.60	1.6	} .68	.024		
		180	1.4	18	20	.53	1.6				
6	27	130	2.1	12	20	1.4	12	} .26	.95		
		180	2.1	18	42	2.4	48				
7	---	140	4.0	29	48	5.8	47	} .33	1.18		
		194	2.0	72	24	3.8	72				
8	26	145	1.3	13	8.8	.31	-3.4	} -2.7	.097		
		195	1.7	7	13	.51	-2.5				
9	23	11	.56	54	69	.63	-3.5	} 3.7	.13	Outward	
		121	-3.4	9	21	1.2	1.1				
		175	-1.5	4.9	7.3	.90	-4.6				

trum. The peak frequency and azimuthal phase velocity (calculated from eq. (2)) are listed for each peak in columns 3 and 4. The next two columns list the root-mean-square (rms) amplitude of each peak in volts. The rms amplitude of the peaks in the density spectrum (column 7) are given in units of  $10^{14}$  per cubic meter. The amplitudes of the potential peaks range from about 10 volts to several hundred volts. Run 4 is an example of a spectrum so turbulent that no separate peaks could be identified. The specific figures illustrating the entries in table IV are identified in the table.

The fluctuation spectrum in the plasma with electrodes 5 and 6 in place, an anode voltage of 2 kilovolts, a neutral background density of  $3.5 \times 10^{11}$  particles per cubic centimeter ( $1.06 \times 10^{-5}$  torr) - run 5 in tables I and IV - is shown in figure 15. The peaks in the cross-power spectrum that have high coherency are at 30 and 180 kilohertz. The mode at 30 kilohertz propagates with an azimuthal phase velocity of  $3.9 \times 10^6$  centimeters per second in the direction of the E/B drift with a radially outward-pointing electric field. The wave at 180 kilohertz propagates with an azimuthal velocity of  $1.4 \times 10^6$  centimeters per second in the same direction. The spectral band from 0 to 75 kilohertz has high coherency and very little jitter in the phase plot, implying the presence of a continuum of eigenmodes. The continuum propagates along with the 30-kilohertz mode. It has an amplitude of about 15 volts rms. The dominant mode at 30 kilohertz is oscillating with an amplitude of 60 volts rms. The power spectrum falls off gradually at 250 kilohertz, where it corresponds to a noise level of about 4.5 volts rms. The radial profile of the floating potential measured with a Langmuir probe indicates that the plasma boundary is subjected to a radially outward-pointing electric field of no less than 90 volts per centimeter. For a magnetic field of 0.67 tesla at the probe, this corresponds to an E/B drift velocity of  $1.3 \times 10^6$  centimeters per second. The magnetic field in the bumpy torus is highly nonuniform both radially and axially. The region in which the probe was located had the lowest magnetic field in the entire containment volume. Any higher magnetic field in the plasma volume will give lower values of the E/B drift velocity, given the electric field measured at the probe location. In all calculations, a magnetic field of 0.67 tesla, corresponding to the region where the floating potential profile and the wave dispersion were measured, was used.

The wave dispersion measured when the sector diametrically opposite to the one containing the probe assembly had an electrode ring (electrode in section 10 only) is shown in figure 16 and corresponds to run 7 in tables I and IV. The coherent modes occur at 140 and 194 kilohertz and propagate with velocities of  $4.0 \times 10^6$  and  $2.0 \times 10^6$  centimeters per second, respectively, in the direction of the E/B drift velocity. The radial electric field for this case was 110 volts per centimeter and points radially outward. It corresponds to an E/B drift velocity of  $1.6 \times 10^6$  centimeters per second.

Figure 17 shows the power spectra of the fluctuations present in the plasma generated with electrodes 1 and 7 in place at a background neutral density of  $7 \times 10^{11}$  particles per cubic centimeter ( $2.1 \times 10^{-5}$  torr) and an anode voltage of 1 kilovolt (run 3 in tables

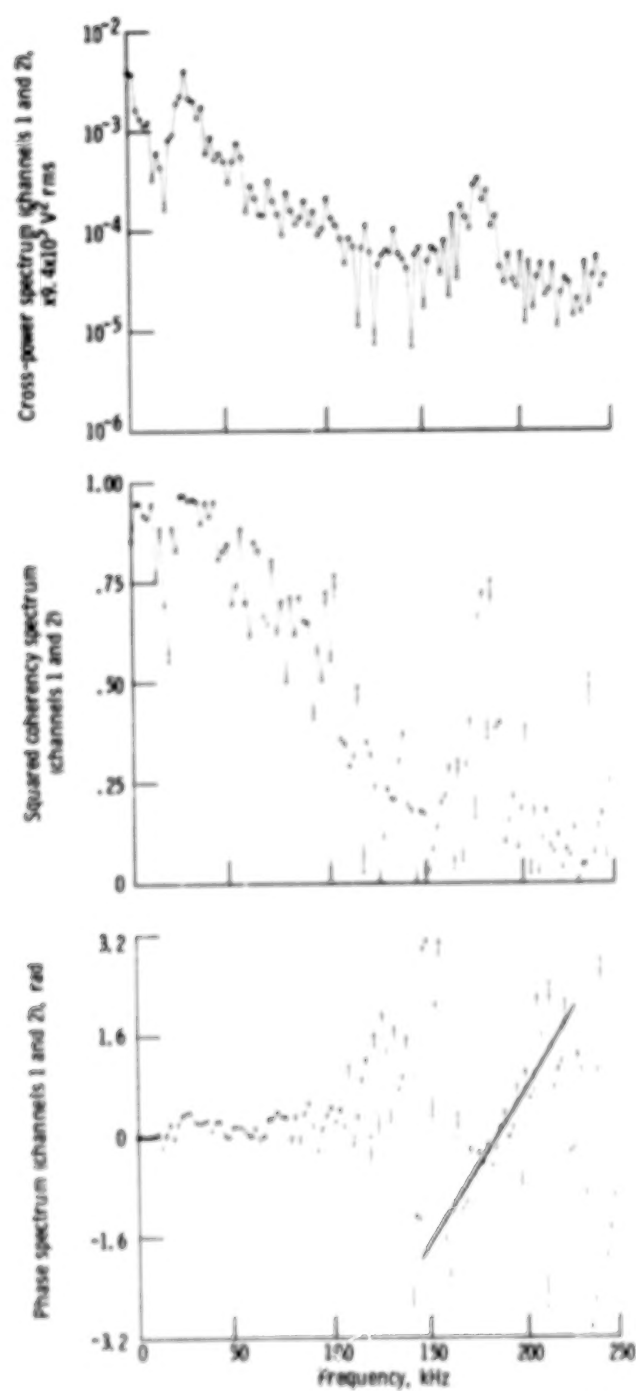


Figure 15. - Azimuthal wave dispersion for run 5 of table I.

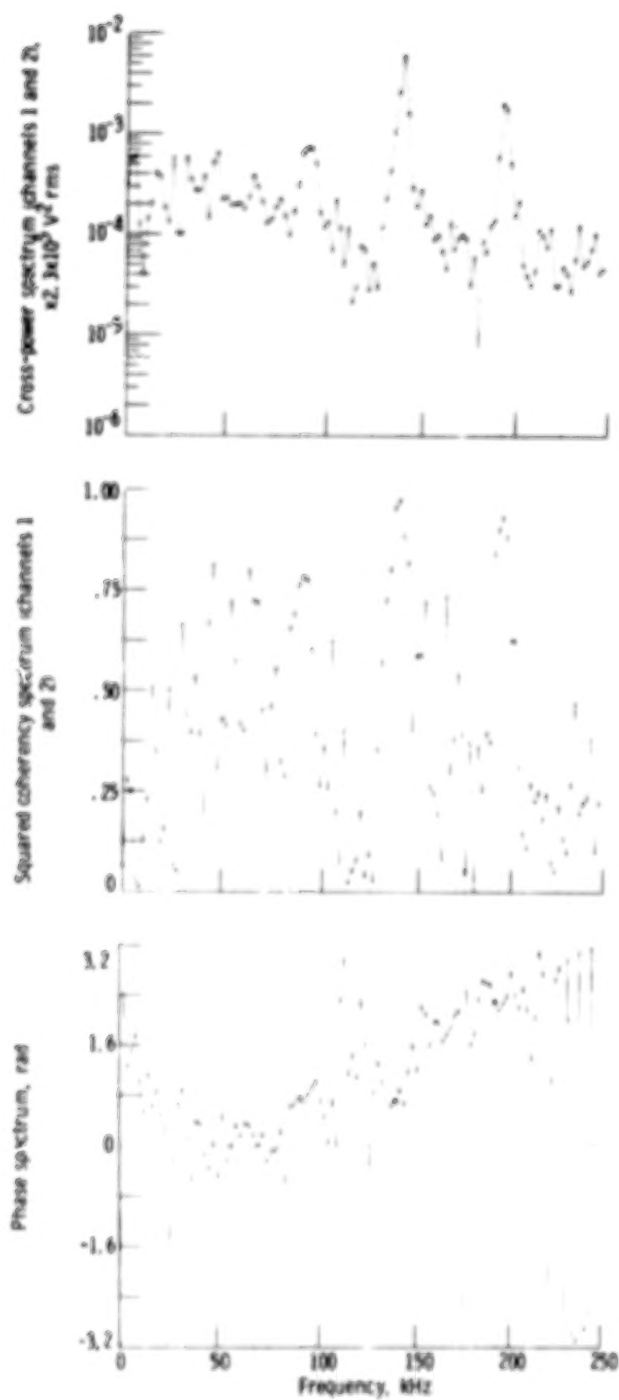


Figure 16. - Azimuthal wave dispersion for run 7 of table 1.

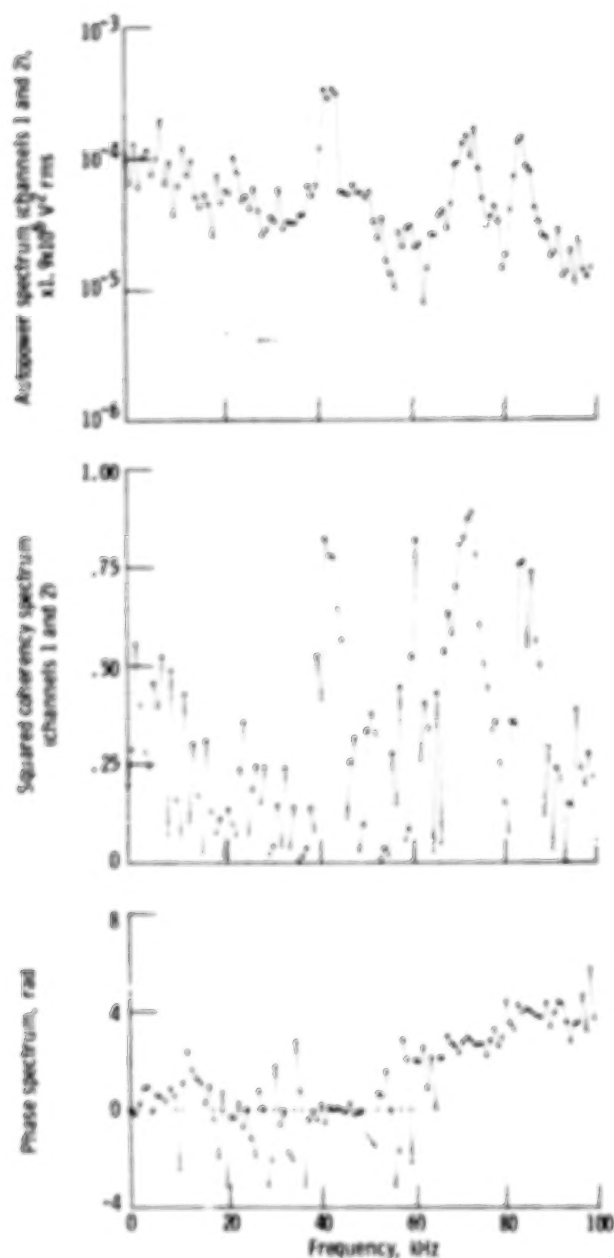


Figure 17. - Azimuthal wave dispersion for run 3 of table 1.

I and IV). The strongest peak with an amplitude of 25 volts rms occurs at 42 kilohertz. The phase spectrum indicates that  $k_{\theta} = 0$  at 42 kilohertz. The two other coherent oscillations present are at 72 and 84 kilohertz. The mode at 72 kilohertz propagates with a velocity of  $5.5 \times 10^5$  centimeters per second in the direction of the E/B drift with a radially outward-pointing electric field. Low coherence in the spectral band 0 to 35 kilohertz indicates the presence of noise. A measured radial electric field of 120 volts per centimeter corresponds to an E/B drift velocity of  $1.8 \times 10^6$  centimeters per second.



## High-Pressure Mode

The wave dispersion when all the electrodes except sector 4 were used to generate the plasma is shown in figure 18 (run 4 in tables I and IV). The coherency plot shows that the spectral band 1 to 10 kilohertz has high coherency, and the phase spectrum shows that  $k_\theta = 0$  in this band. The cross-power spectrum lacks any peaks, though the amplitude of the fluctuations in the 1- to 10-kilohertz band is about 15 volts rms.

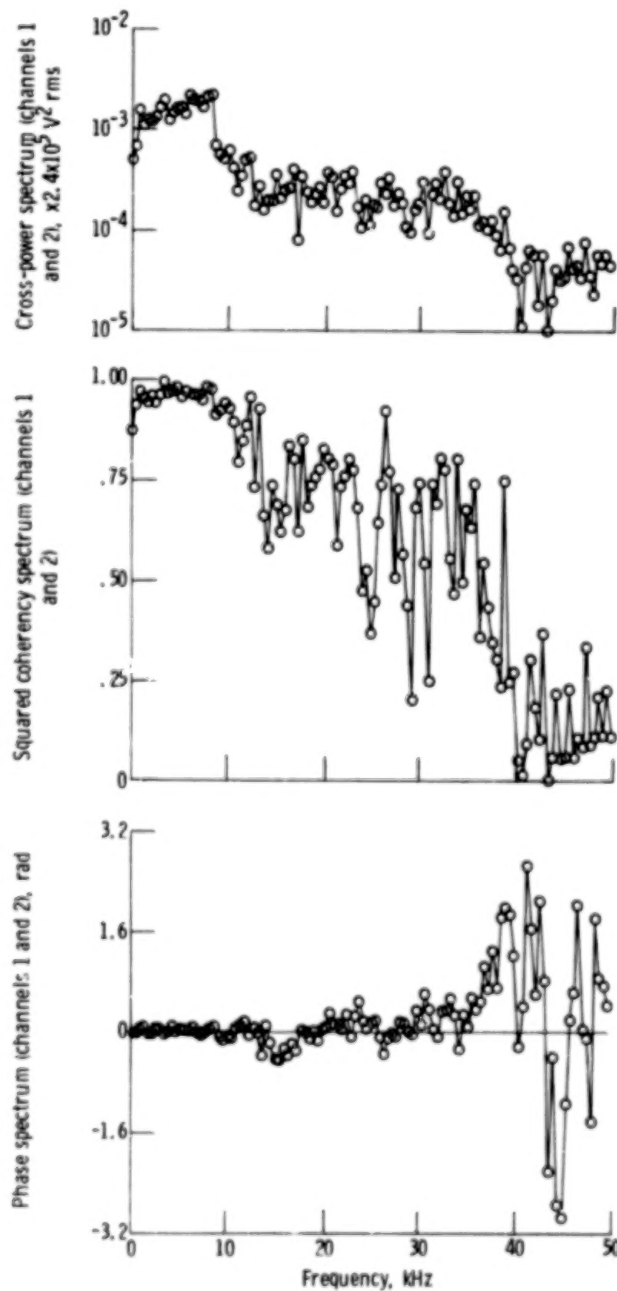


Figure 18. - Azimuthal wave dispersion for run 4 of table I.

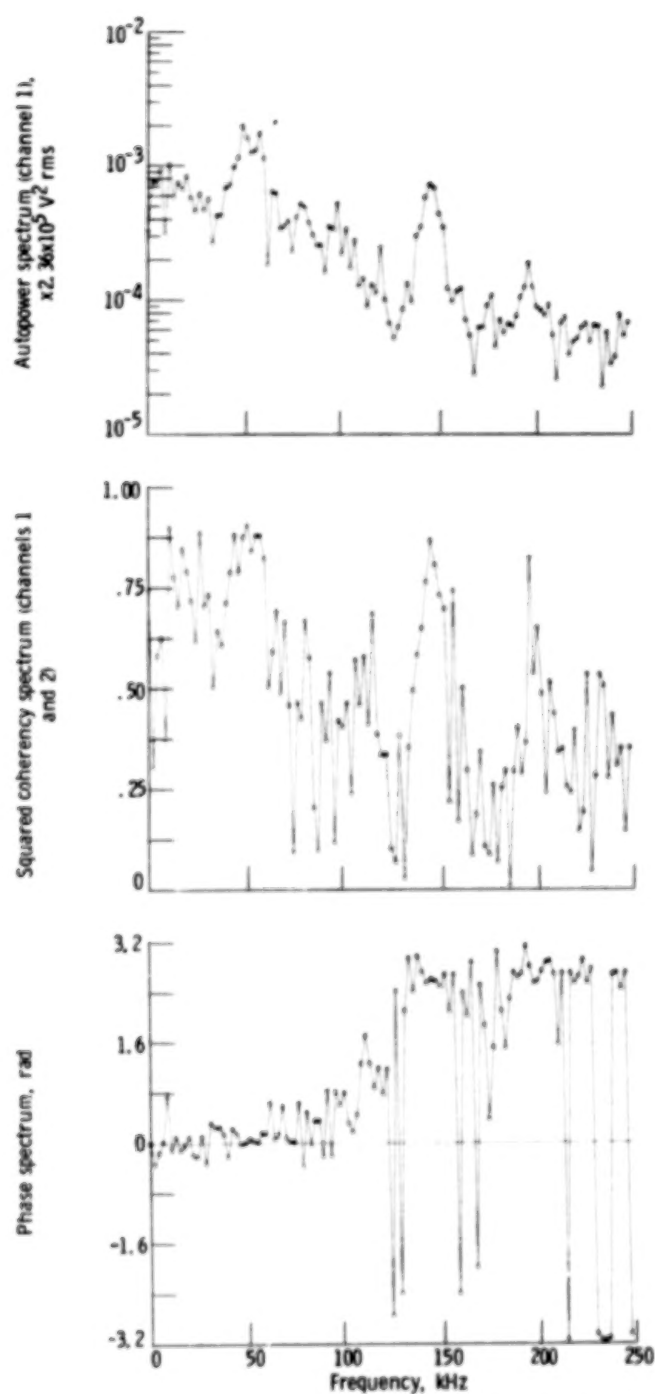


Figure 19. - Azimuthal wave dispersion for run 8 of table II.

The power spectrum falls off gradually between 10 and 50 kilohertz. At 50 kilohertz, the amplitude is about 4 volts rms, the coherency is low, and the phase is jittery - characteristics of noise. Examination of a wider spectral band shows that figure 18 is representative of the fluctuation spectrum with no additional peaks at higher frequencies than those shown. A dc radial electric field of 80 volts per centimeter was present at the probe location, yielding an E/B drift velocity of  $1.2 \times 10^6$  centimeters per second.

Figure 19 shows a case like that of figure 17 except that the neutral background density has been changed to  $1.6 \times 10^{12}$  particles per cubic centimeter ( $4.8 \times 10^{-5}$  torr), run 8 in tables I and IV. The autopower spectrum of channel 1 has peaks at 50, 145, and 195 kilohertz. The mode at 50 kilohertz is characterized by  $k_\theta = 0$ . The waves at 145 and 195 kilohertz are propagating with phase velocities of  $1.3 \times 10^6$  and  $1.7 \times 10^6$  centimeters per second in the direction of the E/B drift with a radially outward-pointing electric field.

## FLUCTUATION-INDUCED PARTICLE TRANSPORT

### Theoretical Considerations

The key ideas underlying our approach to measuring fluctuation-induced transport are described in detail in reference 25. Low-frequency ( $\omega \ll \omega_{ci}$ ) fluctuations are assumed so that a particle's fluctuating velocity may be modeled in terms of an  $\tilde{E}_\perp/B$  drift, where  $\tilde{E}_\perp$  is a fluctuating electric field and B is the static, confining, toroidal magnetic field. The time-averaged particle flux is then given by

$$\langle \tilde{n} \tilde{v} \rangle = \frac{\langle \tilde{n} \tilde{E}_\perp \rangle}{B} = \frac{1}{B} C_{nE}(0) \quad (3)$$

where  $C_{nE}(0)$  is the cross-correlation function between density and electric field fluctuations evaluated for zero time delay. Our goal is to relate  $\langle \tilde{n} \tilde{v} \rangle$  to experimentally observable spectral properties of the fluctuations. To do this we recall that the cross-correlation function between density and potential fluctuations may be expressed in terms of the inverse Fourier transform of the cross-power spectrum between density and electric field fluctuations  $P_{nE}(\omega)$ :

$$C_{nE}(\tau) = \langle \tilde{n}(t) \tilde{E}_\perp(t + \tau) \rangle = \int_{-\infty}^{\infty} P_{nE}(\omega) e^{-i\omega\tau} d\omega \quad (4)$$

Substituting equation (4) into equation (3) yields

$$\langle \tilde{n}\tilde{v} \rangle = \frac{2}{B} Re \int_0^\infty P_{nE}(\omega) d\omega \quad (5)$$

where the time-averaged particle flux is expressed as an integral over all frequencies of the real part of the cross-power spectrum between density and electric field fluctuations.

In the NASA Lewis bumpy-torus experiment we have the capability to measure potential rather than electric field fluctuations. To the extent that the quasi-static approximation  $\tilde{E}_\perp = -\nabla_\perp \tilde{\phi}$  holds, the cross-power spectrum between density and electrical field fluctuations  $P_{nE}(\omega)$  may be expressed in terms of the cross-power spectrum between density and potential fluctuations  $P_{n\phi}(\omega)$  (ref. 25) as follows:

$$P_{nE}(\omega) = -ik_\perp(\omega) P_{n\phi}(\omega) \quad (6)$$

where  $k_\perp(\omega)$  is the perpendicular wave number.

Substituting equation (6) back into equation (5) yields the final result

$$\langle \tilde{n}\tilde{v} \rangle = \int_0^\infty T(\omega) d\omega \quad (7a)$$

which states that the time-averaged particle flux is given by an integral over all frequencies of the transport spectral density function  $T(\omega)$ . The quantity  $T(\omega)$  is defined as

$$T(\omega) \equiv \frac{2}{B} k_\perp(\omega) Q_{n\phi}(\omega) \quad (7b)$$

where the quadrature spectrum  $Q_{n\phi}(\omega)$  is defined as the imaginary part of  $P_{n\phi}(\omega)$ . The factor 2 in equation (7b) takes into account the "negative frequency" contributions to the particle transport. ( $T(\omega)$  is an even function of frequency.) The function  $T(\omega)$  is a "transport spectral density function" in that its dimensions are number of particles per unit time, per unit area, and per unit radian frequency. Thus a visual inspection of a plot of  $T(\omega)$  not only will indicate which parts of a fluctuation spectrum are contributing to transport, but also will indicate in a quantitative way how much transport is associated with each spectral band.

Our approach in generating the transport spectral density function is as follows: First, the signals (channel 1 and channel 2) from the two capacitive probes displaced  $30^\circ$

apart in azimuth are digitized and the perpendicular wave number  $k_{\perp}(\omega)$  is determined by using the procedures reviewed in the section AZIMUTHAL DISPERSIVE CHARACTERISTICS OF PLASMA. Next the signal from the Langmuir probe (channel 3) is digitized and its Fourier transform computed. From the Fourier transforms of the density fluctuation and the potential fluctuation signal in channel 1, the quadrature spectrum  $Q_{n\phi}(\omega)$  is computed by using the procedures described in reference 23. The transport spectrum<sup>2</sup> is then generated by carrying out the multiplication indicated in equation (7b).

Although equation (7b) is useful in terms of how to compute a transport spectrum, an alternative formulation is advantageous in terms of understanding which effects result in large or small amounts of transport. For example, it is shown in reference 25 that the transport due to a small band of frequencies centered at  $\omega$  is given by

$$T(\omega) = \frac{k_{\perp}(\omega)}{B} n_{\text{rms}}(\omega) \phi_{\text{rms}}(\omega) \sin[\alpha_{n\phi}(\omega)] |\gamma_{n\phi}(\omega)| \quad (8)$$

Therefore, the transport associated with this band of frequencies centered about  $\omega$  depends on the following factors: the product of the rms values of density and potential fluctuations, the sine of the phase angle  $\alpha_{n\phi}(\omega)$  between the density and potential fluctuations, and the degree of mutual coherence  $|\gamma_{n\phi}(\omega)|$  between the density and potential fluctuations in the spectral band under consideration. The factor  $k_{\perp}(\omega)$  appears since  $|k_{\perp}(\omega) \phi_{\text{rms}}(\omega)| \simeq \tilde{E}_{\perp, \text{rms}}(\omega)$ , and our model assumes  $\tilde{v} = \tilde{E}_{\perp}/B$ .

In subsequent figures, computer-generated plots of transport spectra are shown in the lower right corner. Either  $n_{\text{rms}}^2(\omega)$ , the autopower spectrum of channel 3, or  $n(\omega)\phi(\omega)|\gamma_{n\phi}(\omega)|$ , the cross-power spectrum between channels 1 and 3, is plotted in the upper left corner. The phase-difference spectrum  $\alpha_{n\phi}(\omega)$  for density and potential fluctuations is plotted in the lower left corner and corresponds to the phase spectrum between channels 1 and 3. Since the transport depends on  $\sin \alpha_{n\phi}(\omega)$ , values of  $\alpha_{n\phi}(\omega)$  near  $\pm 90^\circ$  are optimum in terms of transport. Finally, the square of the degree of mutual coherence between density and potential fluctuations  $|\gamma_{n\phi}(\omega)|^2$  is plotted in the upper right corner and corresponds to the square of the degree of mutual coherence between channels 1 and 3. As explained in reference 25, the degree of mutual coherence between density and potential fluctuations enters into equation (8) because we are considering a polychromatic case rather than a monochromatic case. In the monochromatic case the

<sup>2</sup>Since the data have been digitized, we actually plot a transport spectrum (Number of particles/Area·Time) not a transport spectral density function. To determine the total transport associated with a given fluctuation spectrum, we sum, rather than integrate, the transport spectrum over all frequency values.

degree of mutual coherence would be unity.<sup>3</sup>

The transport spectrum  $T(\omega)$  is a real quantity and may be either positive or negative depending on whether the transport is in the inward or outward direction. Equation (8) indicates that only two quantities determine the sign of  $T(\omega)$  and hence the direction of transport: The first quantity is the phase difference  $\alpha_{n\phi}(\omega)$  between density and potential fluctuations. If  $\alpha_{n\phi}(\omega)$  changes sign,  $T(\omega)$  changes sign since  $T(\omega)$  is proportional to  $\sin \alpha_{n\phi}(\omega)$ . The second quantity determining the sign of  $T(\omega)$  is the sign of  $k_{\perp}(\omega)$ , which in effect determines the direction of the fluctuating electric field  $\tilde{E}_{\perp}$  in equation (3).

### Low-Pressure Mode

The transport spectrum when all the electrodes except that in sector 4 were in place, and with the electrodes biased to 1 kilovolt at a neutral background density of  $7 \times 10^{11}$  particles per cubic centimeter ( $2.1 \times 10^{-5}$  torr), is shown in figure 20 (run 2 in tables I and IV). This figure is a plot of the cross-power spectrum, squared coherency spectrum, phase spectrum, and transport spectrum obtained from the probes in channels 1 and 3. The transport is radially inward in this case. The cross-power spectrum is dominated by a peak at 15 kilohertz that corresponds well with a similar peak in the coherency spectrum. This implies that there is a coherent wave mode in the potential and density fluctuations. The phase spectrum reveals that at 15 kilohertz the phase difference between density and potential fluctuations is  $120^{\circ}$ . As the transport spectrum indicates, there is negligible transport in the whole spectral band outside the peak at 15 kilohertz. Keeping all other parameters the same, we changed the anode voltage to 2 kilovolts (run 1 in tables I and IV). Figure 21 shows the corresponding transport spectrum, which is also radially inward. The transport spectrum and the cross-power spectrum show that the coherent wave that causes large amounts of transport now occurs at 20 kilohertz. The phase difference between density and potential fluctuations is now  $40^{\circ}$  and the amplitude of the peak in the cross-power spectrum is again 22 decibels above the noise level. The spectral band from 30 to 100 kilohertz has low coherency and a jittery phase spectrum - characteristics of noise. In this frequency interval, the transport spectrum indicates very little transport of plasma. Figure 22 shows the dispersion spectra for the conditions corresponding to figure 21.

---

<sup>3</sup>Other properties of coherency spectra are reviewed in ref. 24. In particular, low values of  $|\gamma_{n\phi}(\omega)|$  may be due to noise in the system, a departure from a linear relation between density and potential fluctuations, and/or so-called multiple inputs.

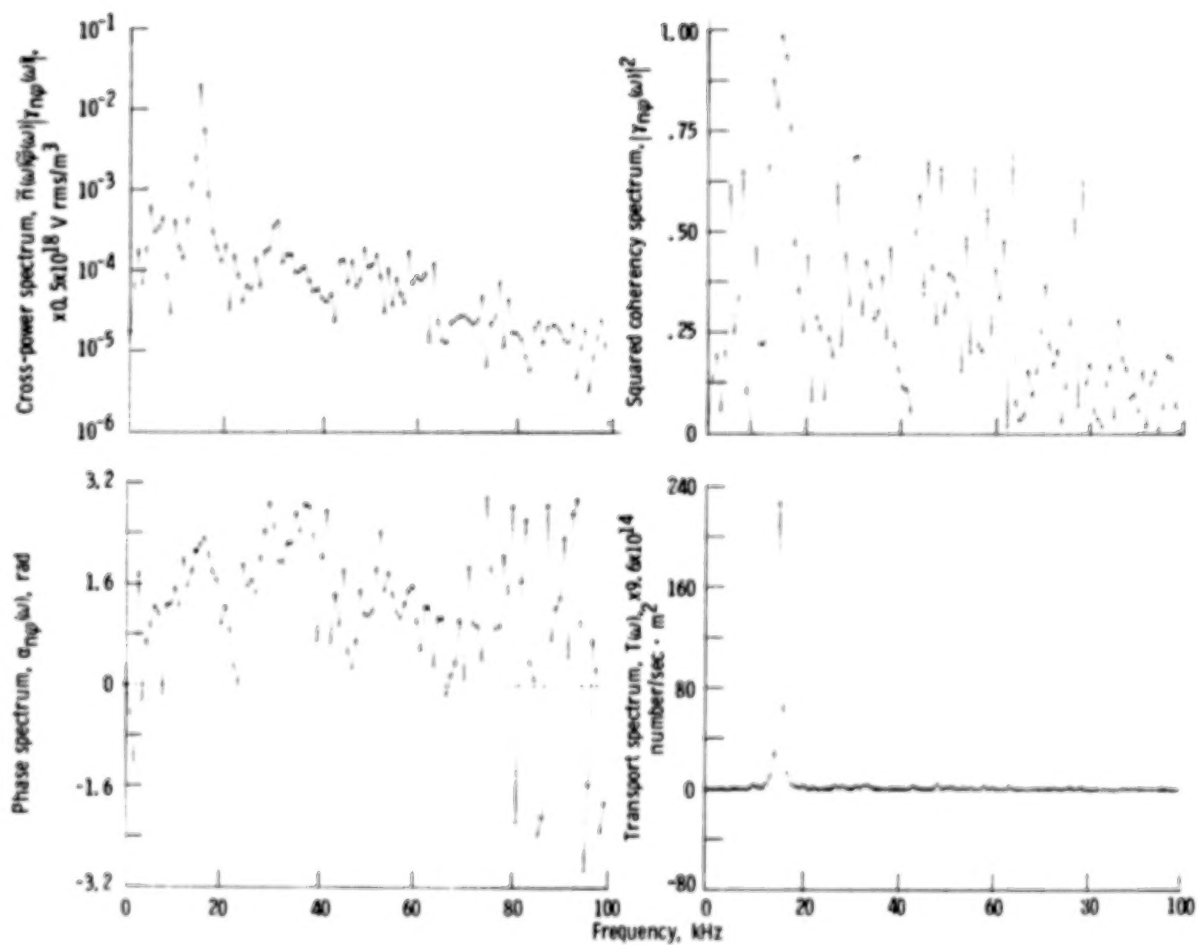


Figure 20. - Transport spectrum for run 2 of table I.

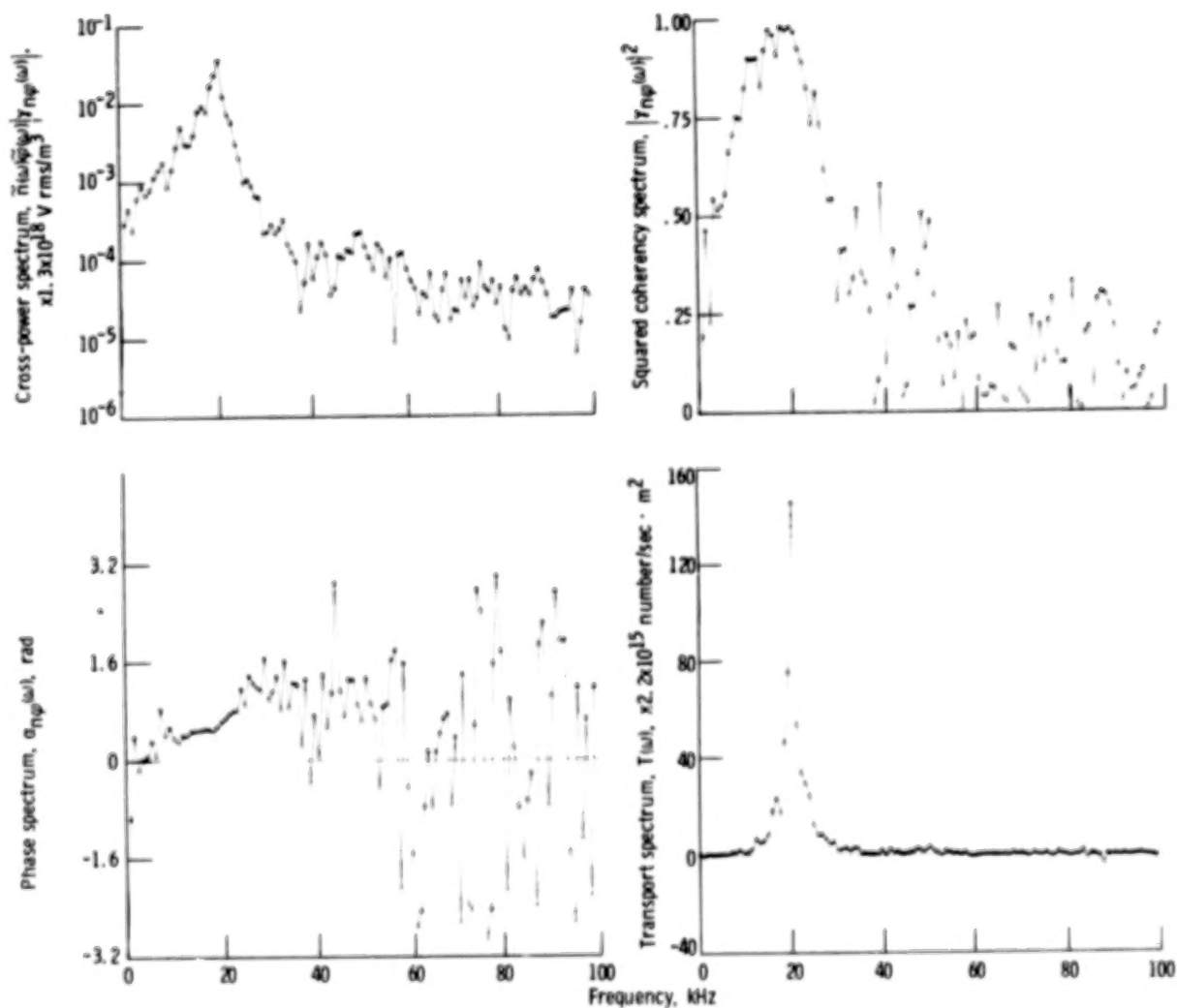


Figure 21. - Transport spectrum for run 1 of table 1.



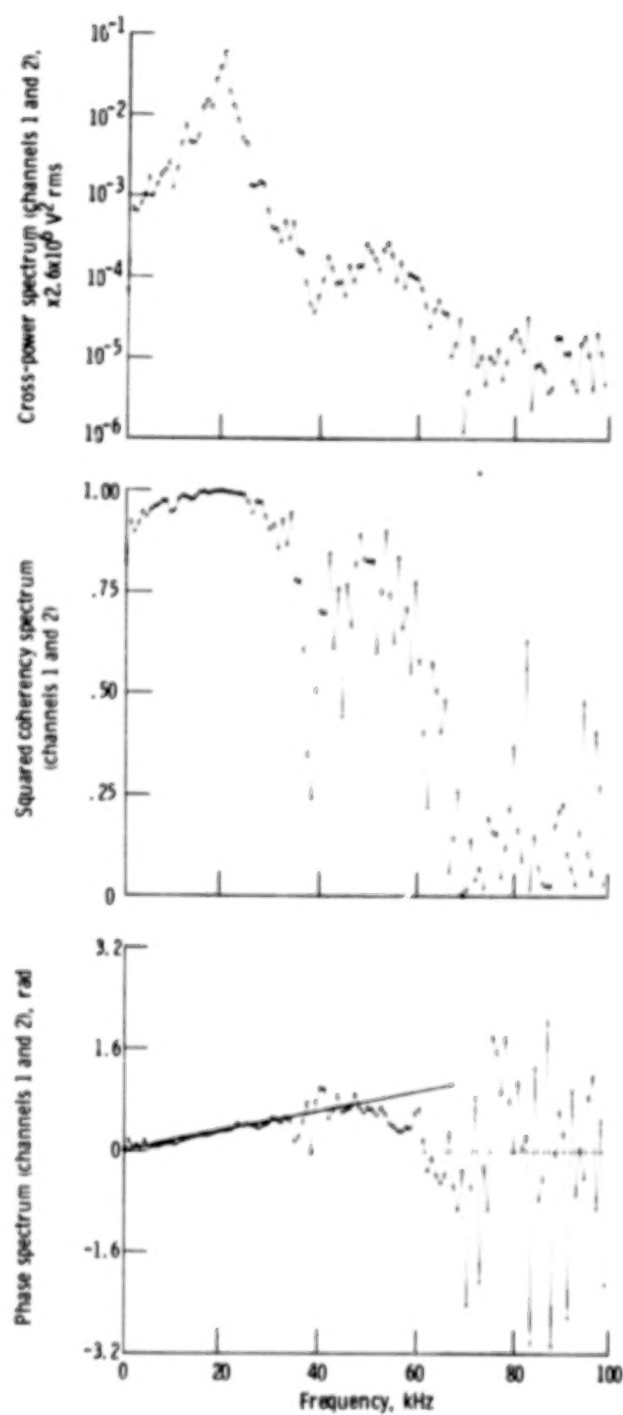


Figure 22. - Dispersion spectra for run 1 of table 1.

These indicate a very coherent wave propagating at  $1.6 \times 10^6$  centimeters per second at 20 kilohertz.

To study the transport with different electrode ring configurations, we kept the probe assembly fixed in sector 4 and changed the location of the electrodes from sectors 3 and 9 (figs. 23 and 24 and run 9 in tables I and IV) to sectors 1 and 7 (fig. 25 and run 3 in tables I and IV). The neutral background density was kept at  $7 \times 10^{11}$  particles per cubic centimeter ( $2.1 \times 10^{-5}$  torr) and the anode voltage, at 1 kilovolt. When the nearest electrode is one sector away, the cross spectrum (fig. 23) has peaks at 121 and 178 kilohertz, which correspond to high coherency in the squared coherency spectrum. There is hardly any transport at 121 kilohertz because of the small phase difference between the potential and density fluctuations. Figure 24 shows the dispersion spectra for the conditions in figure 23. These spectra indicate a relatively coherent disturbance propagating at  $0.56 \times 10^6$  centimeters per second at 11 kilohertz. The net transport was radially inward in this case. The transport spectrum when the electrodes are three sectors away on each side of the probe is shown in figure 25. The net transport at the probe location was outward in this case. The autopower spectrum

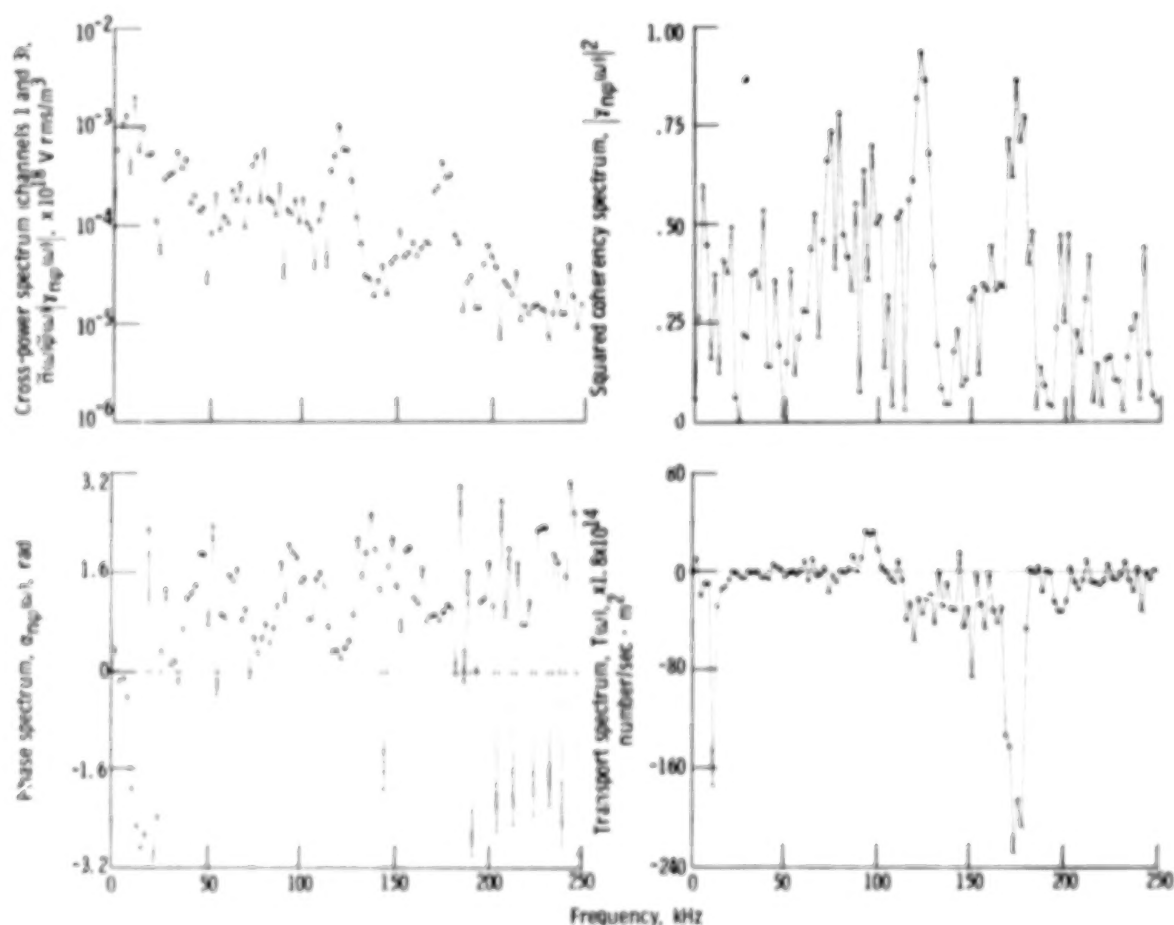


Figure 23. - Transport spectrum for run 9 of table I.

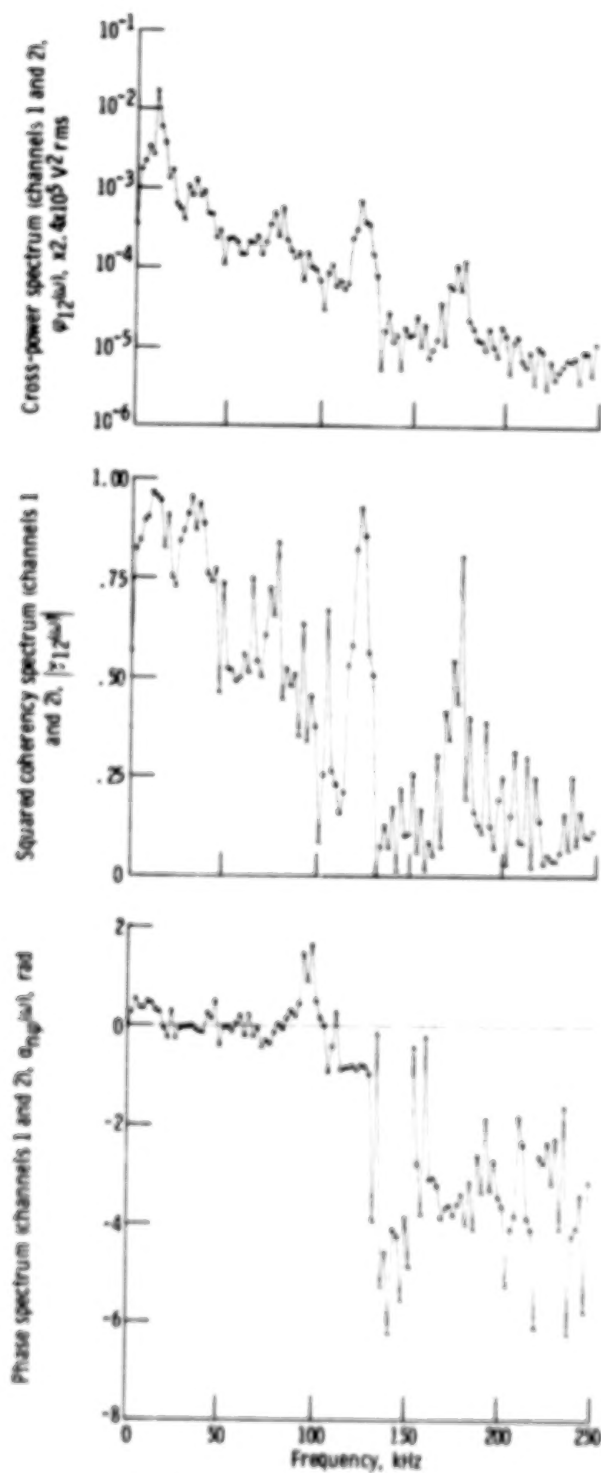


Figure 24. - Dispersion spectra for run 9 of table 1.

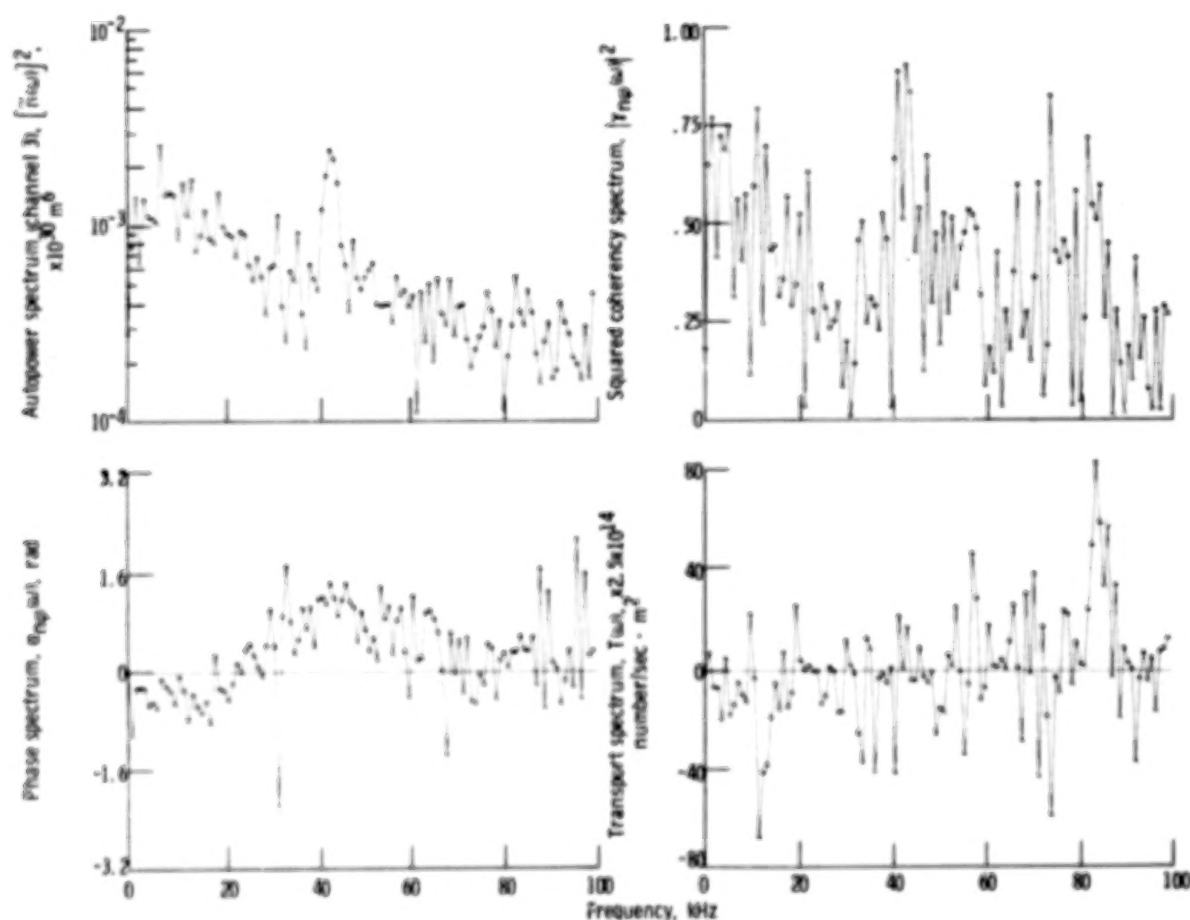


Figure 25. - Transport spectrum for run 3 of table I.

of the ion density fluctuations has a dominant peak only at 42 kilohertz. However, the capacitive probe at the same point in the plasma picks up signals at 42, 72, and 84 kilohertz, as shown in figure 17. The disturbance at 42 kilohertz is characterized by  $k_\theta = 0$ , since the value of  $\theta_{12}(\omega)$  is approximately zero at this frequency (fig. 17). It is immediately noticeable that an approximately zero  $k_\theta$  in the transport equation (eq. (7b)) results in very low transport at 42 kilohertz in figure 25.

### High-Pressure Mode

The transport spectrum in the high-pressure mode for the conditions of figure 25 is shown in figure 26 (run 8 in tables I and IV). The density fluctuation spectrum has peaks at 145 and 195 kilohertz. The net radial transport is outward in this case. Even though in figure 26 the amplitude of the disturbance at 145 kilohertz is smaller than that at 195 kilohertz, the absolute amount of transport is more at 145 kilohertz. The reason for this is that at 145 kilohertz the phase difference between density and potential is

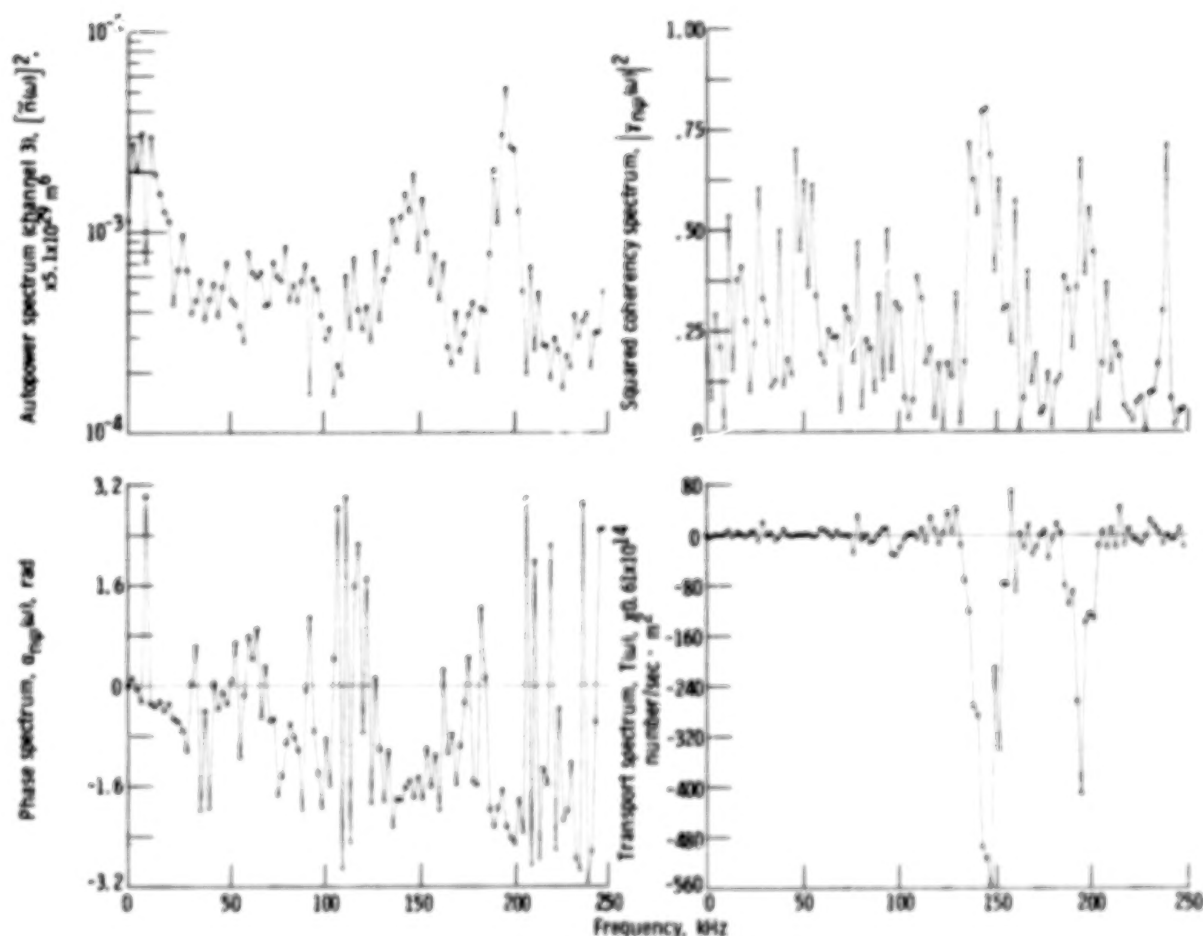


Figure 26. - Transport spectrum for run 8 of table 1.

optimum ( $90^\circ$ ) for maximum transport. The transport associated with the 145- and 195-kilohertz peaks is negative since, at these frequencies, the phase difference between density and potential fluctuations is negative.

Figure 27 shows the transport spectrum present in the plasma when the plasma was generated by an electrode in a sector (10) diametrically opposite the probe assembly. Disturbances that have peaks in the cross-power spectrum and high coherency are at 130 and 180 kilohertz. The dominant transport occurs at 180 kilohertz, and the net transport is radially inward. The phase difference between density fluctuations and potential fluctuations is an optimum of  $90^\circ$ . Figure 28 shows the dispersion spectra for the conditions of figure 27. These spectra indicate that virtually all disturbances up to 250 kilohertz are propagating at  $2.1 \times 10^6$  centimeters per second.

Figure 29 illustrates the fourth run in tables I and IV, the dispersive characteristics of which are shown in figure 18. In this case, the coherency is low and the transport is very low in magnitude and quite turbulent in the sense of having no dominant peaks in the spectrum. A summation over all frequency bands of the transport spectrum yields a net inward transport of particles.

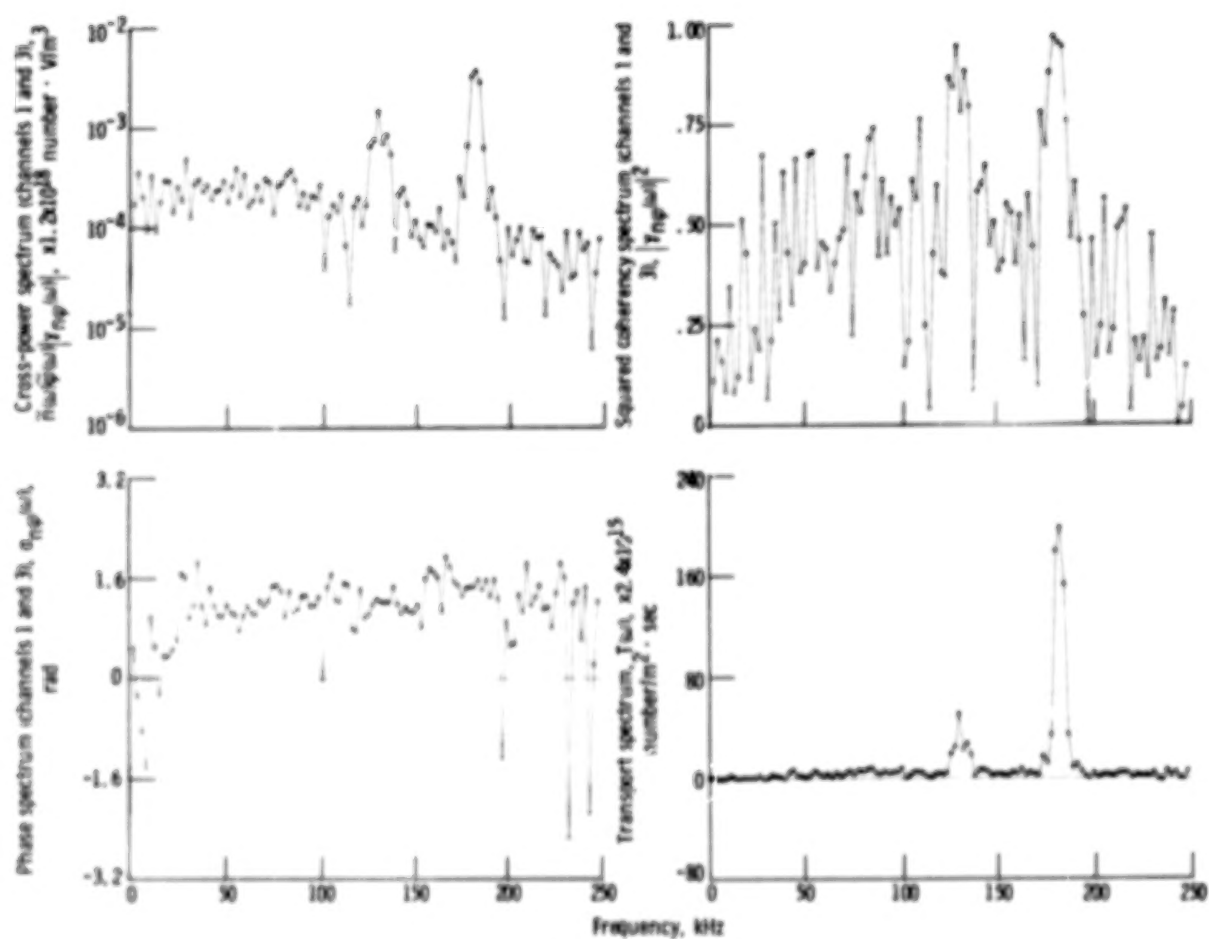


Figure 27. - Transport spectrum 'r' run 6 of table 1.

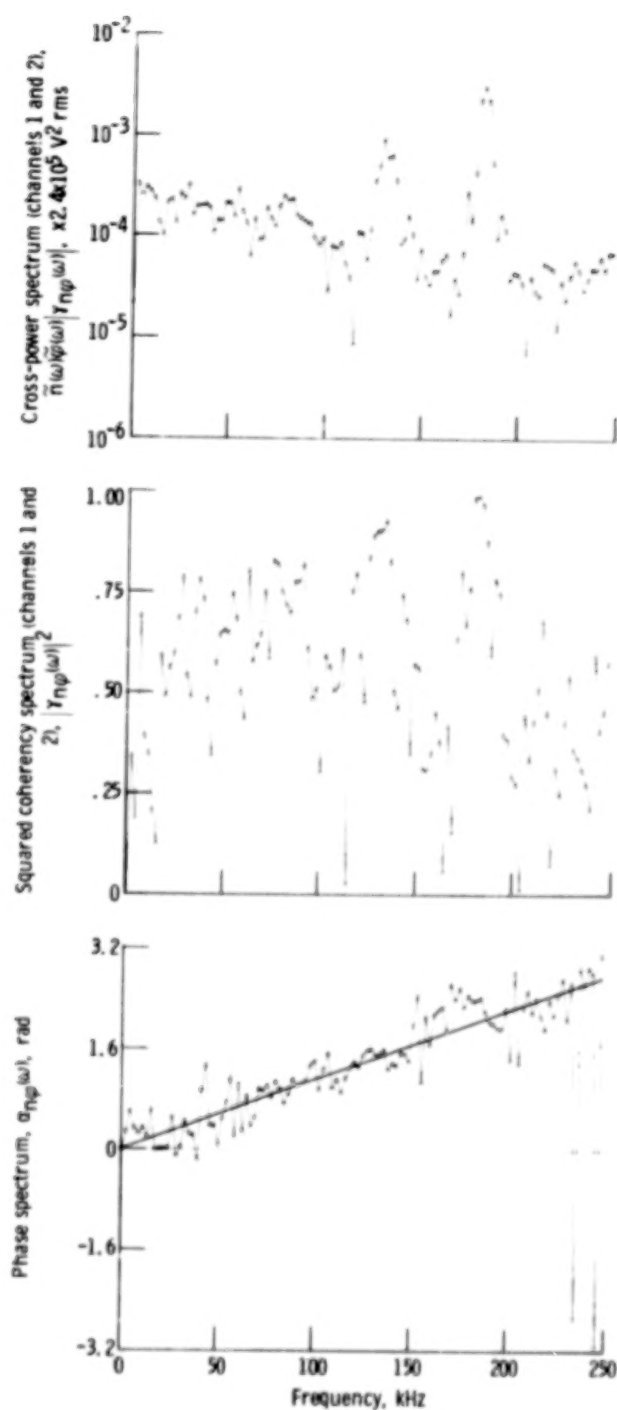


Figure 28. - Dispersion spectrum for run 6 of table 1.

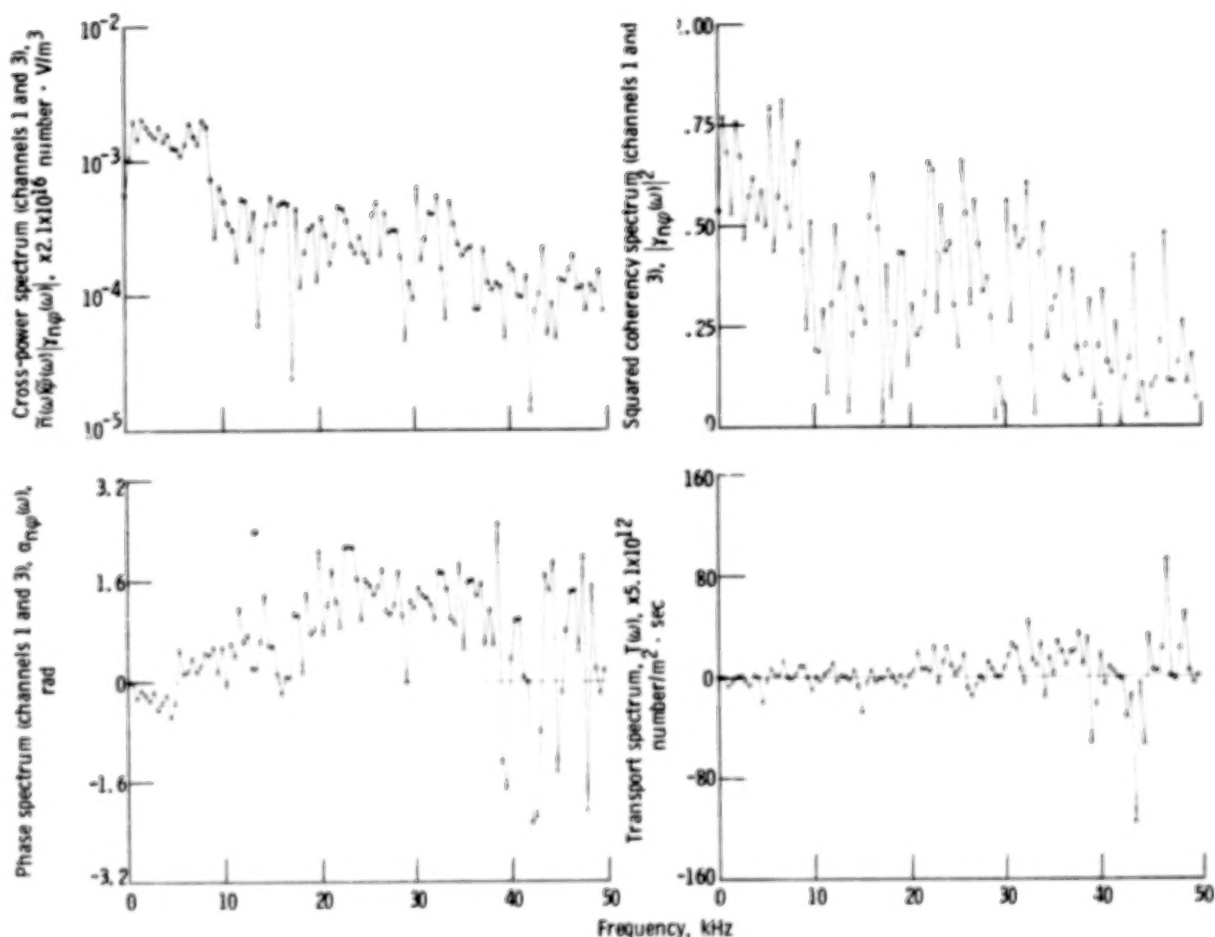


Figure 29. - Transport spectrum for run 4 of table I.

### Total Ion Transport Rates

The last four columns of table IV contain information about the absolute rates of transport as measured with this technique. The first of these (column 8) contains the transport rate associated with each of the dominant peaks that are evident in the transport spectrum. In the third and fourth runs, no peaks appear above the background turbulent noise, and in the last five runs there is more than one peak in the spectrum. Positive values of transport are radially inward, and negative values are radially outward. The total cumulative transport summed over all frequency bands of the spectrum (column 9) represents the flux of ions at the probe. In collecting the raw data, care was taken to assure that there was no significant fluctuation activity at higher frequencies that might have contributed to the transport. The last column gives the direction of the total transport at the probe.

Charged particles are lost from the plasma at a total rate equal to the current drawn



by the power supply since previous work has shown that no ambipolar currents flow to the electrodes (ref. 4). This total current can be compared with the total, cumulative transport rate only if it is assumed that the probes were located at a typical position. This assumption is not valid since the magnetic field at the probe was weaker than anywhere else in the plasma volume, the probes were inside the plasma boundary rather than on or outside it, and the magnetic field and plasma properties vary both around the minor circumference of the plasma and axially along the magnetic field lines.

Although these factors mitigate against a comparison of the measured transport rates with the electrode current, it is nonetheless interesting to do so. The surface area of the bumpy-torus plasma is 2.23 square meters. If this area is used to convert the transport rates in column 9 of table IV to current flows, the currents shown in column 10 result. Figure 30 plots the measured electrode current from table I as a function of the calculated transport current from table IV. The transport currents are generally within an order of magnitude of the measured currents, about as good agreement as can be expected in view of the nonuniformity of the plasma about the major and minor circumferences of the plasma.

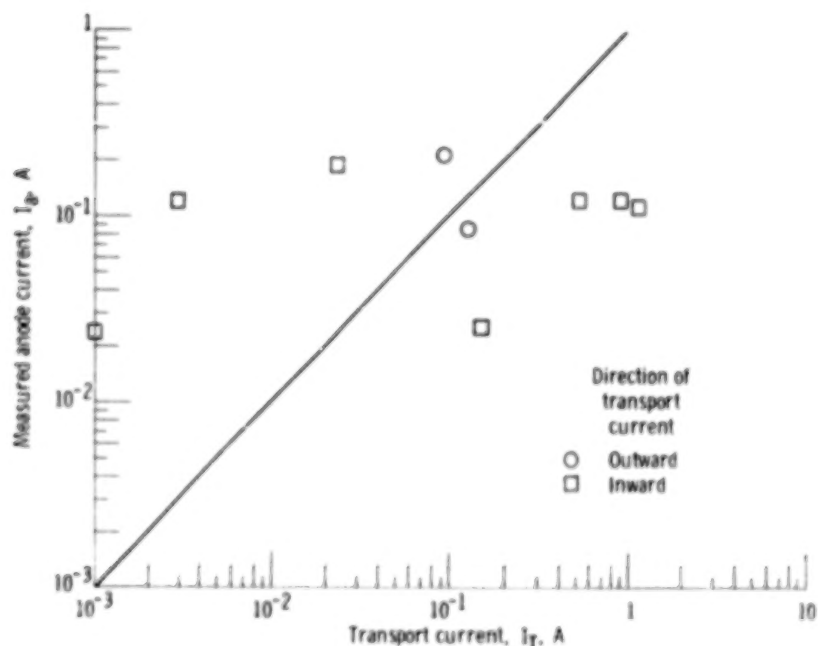


Figure 30. - Measured transport current as a function of electrode current flowing to power supply for experimental runs tabulated in table I.

## DISCUSSION

This report has described the first application of a technique by which the radial particle flux in a hot-ion, steady-state plasma can be measured directly. These data were exploratory and no attempt was made to obtain parametric variations of the dispersion or transport characteristics of the plasma. A wide range of phenomena have been revealed, including rotating disturbances that move with velocities comparable to the E/B drift velocity, transport that is radially inward or outward, and radial transport that is associated with random turbulence as well as with strong coherent peaks in the fluctuation spectra.

The probability density functions of the fluctuating density and potential amplitude are valuable as crosschecks for signal saturation of the raw data. When signal saturation occurs, it is very evident from the large, delta-function-like wings at the extreme edges of the probability density function. The distribution functions of both density and potential generally had a kurtosis of about 3.0, which is characteristic of Gaussian random noise, and nonzero values of skewness, which result from the cusplike waveforms that have been observed in this plasma (refs. 2 and 3). (Random Gaussian waveforms have zero skewness.) The first run in table III is an example in which the raw waveform was very coherent and periodic, with essentially zero skewness (a sinusoidal signal) and kurtosis appropriate to a sinusoid.

When the operating conditions were varied, the plasma exhibited electrostatic potential fluctuations (1) at a set of discrete frequencies, (2) at a continuum of frequencies, and (3) as incoherent turbulence. The coherent discrete modes propagated azimuthally in the direction of the E/B drift, with an electric field that usually pointed radially outward between the plasma and the magnet dewars. Electric fields in the core of the plasma could not be measured with Langmuir probes. A nonperturbing technique, such as ion beam probing, may be required to yield the potential profile in the core of the plasma.

In several runs (of which figs. 15 and 19 are characteristic examples), coherent, discrete modes with  $k_\theta = 0$  have been observed. In such cases, there is a very large peak in the low-frequency potential fluctuation spectrum (below 100 kHz), but there is essentially no time delay between the fluctuations at the site of the two probes. This oscillation of the plasma in unison may be a manifestation of the continuity-equation oscillation, which has been observed in a similar plasma (ref. 26). The possibility that the probes are seeing a radially or axially propagating wave cannot be ruled out on the basis of the data taken for this report, but previous work (ref. 3) demonstrates that coherent low-frequency phenomena, in phase around the major circumference of the torus, do occur. A measurement of  $k_\parallel$  and  $k_r$  will be helpful in confirming the presence of the continuity-equation oscillation in this plasma.

The data on the particle transport spectrum revealed a wide variety of phenomena:

- (1) All transport occurring in a single, sharp peak representing radially inward transport (figs. 20 and 21)
- (2) Transport occurring in two or more peaks, one carrying particles inward and one outward (fig. 23)
- (3) Spectra with two peaks, both carrying particles inward (fig. 27)
- (4) Spectra with two peaks both carrying particles outward (fig. 26)
- (5) Spectra with no prominent peaks, in which the total transport is small and caused by a continuum of turbulent fluctuations (figs. 25 and 29)

Particle transport was radially inward for a majority of the cases examined, an interesting result. This inward transport could be caused by the strong radial and azimuthal electric fields associated with the rotating spokes in the plasma (ref. 3) and may be prevalent in the sector in which the probe was located because there was no electrode ring in that sector, for the data discussed in this report. The transport calculated from the model of reference 25 appears to account for substantially all the particle flux intercepted by the anode rings and the walls. The data in figure 30 indicate that the magnitude of the transport currents, if the probe position is typical of the entire surface of the plasma, is within order-of-magnitude agreement with the currents actually flowing to the power supply.

## CONCLUSIONS

Simultaneous density and potential fluctuation data have been taken in a hot-ion, steady-state, bumpy-torus plasma subject to strong, crossed electric and magnetic fields. The statistical properties of the density and potential fluctuations, the dispersion of the propagating disturbances in the electrostatic potential, and the radial transport spectrum have been calculated. The transport spectrum is based on the model presented by Powers, according to which all radial transport is due to E/B drift caused by potential fluctuations and the resulting electric fields. All measured and calculated quantities, including the potential and density amplitudes and the transport rate, were obtained in absolute units.

At low frequencies (below 100 kHz), a nonpropagating azimuthal mode was observed with  $k_\theta = 0$ . This may be related to the continuity-equation oscillation, which is known to have  $k_\theta = 0$ . Additional measurements are needed of  $k_r$  and  $k_\parallel$  to unambiguously identify this azimuthal mode. The azimuthally rotating spokes had velocities consistent with the E/B drift velocity at the probe. These rotating spokes were often associated with the peaks in the radial particle transport spectrum. The peaks for which  $k_\theta = 0$  did not have significant transport associated with them.

The most surprising feature of the radial transport of ions is that much of it was radially inward in this plasma. The model of Powers appears to account for all the transport in this plasma, because the calculated radial transport rates are in order-of-magnitude agreement with the electrode currents actually drawn from the plasma. The highest rates of radial transport were associated with sharp, coherent peaks in the transport spectrum, and the transport associated with random, turbulent spectra without peaks was much smaller in magnitude.

The exploratory data reported herein have proven the basic value of the radial transport model given by equation (3) and of the hardware and software systems developed to acquire and analyze the required data. Future work along these lines should include a study of parametric variations, including the transport rate as a function of electrode voltage, plasma density, and other independent variables that affect the plasma characteristics.

Lewis Research Center,

National Aeronautics and Space Administration,

Cleveland, Ohio, April 4, 1978,

506-25.

# APPENDIX - SYMBOLS

B	magnetic field strength, T
C	cross-correlation function, eq. (3)
E	electric field strength, V/m
E(A, B)	expected value of A, B
e	electronic charge, C
f	amplitude probability function
k	wave number, $m^{-1}$
m( $\omega$ )	mode spectrum of propagating waves
n	number density, $cm^{-3}$
P <sub>ii</sub> ( $\omega$ )	autopower spectrum
P <sub>ij</sub> ( $\omega$ )	cross-power spectrum
Q( $\omega$ )	quadrature spectrum
R	radius from plasma axis, m
$\Delta R$	distance between probes, m
T	kinetic temperature, eV
T( $\omega$ )	transport spectral density function
t	time, sec
V	voltage, V
v	velocity, m/sec
x	fluctuation amplitude
$\alpha$	phase angle, rad
$\gamma_{ij}(\omega)$	coherence spectrum of signals i, j
$\theta_{ij}$	phase spectrum
$\Delta\bar{\theta}$	angular distance between probes
$\lambda$	wavelength, m
$\sigma(p)$	"p" <sup>th</sup> moment of distribution function, eq. (1)
$\tau$	time interval, sec
$\Phi$	Fourier transform of potential, V

$\phi$  potential, V  
 $\omega$  frequency, rad/sec

**Subscripts:**

a anode  
 ci ion cyclotron  
 e electrons  
 i ions  
 n particle number density  
 p probe  
 $p_\phi$  phase velocity in azimuthal direction  
 r radial direction  
 rms root mean square  
 $\theta$  azimuthal direction  
 $\phi$  potential  
 $\parallel$  parallel to magnetic field  
 $\perp$  perpendicular to magnetic field  
 1 capacitive probe, channel 1  
 2 capacitive probe, channel 2  
 3 Langmuir probe, channel 3

**Superscripts:**

— time-averaged value  
 $\sim$  fluctuating value  
 $*$  complex conjugate

## REFERENCES

1. Roth, J. Reece; et al.: Characteristics and Performance of a Superconducting Bumpy-Torus Magnet Facility for Plasma Research. NASA TN D-7353, 1973.
2. Roth, J. Reece; Gerdin, Glenn A.; and Richardson, Richard W.: Characteristics of the NASA Lewis Bumpy-Torus Plasma Generated with Positive Applied Potentials. NASA TN D-8114, 1976 (see also IEEE Trans. Plasma Sci., vol. PS-4, no. 3, Sept. 1976, pp. 166-176).
3. Roth, J. Reece; and Gerdin, Glenn A.: Characteristics of the NASA Lewis Bumpy-Torus Plasma Generated with High Positive or Negative Applied Potentials. NASA TN D-8211, 1976 (see also Plasma Phys., vol. 19, no. 5, May 1977, pp. 423-446).
4. Roth, J. Reece: Factors Affecting Ion Kinetic Temperature, Number Density, and Containment Time in the NASA-Lewis Bumpy Torus Plasma. NASA TN D-8466, 1977.
5. Singh, Chandra M.; Krawczonek, Walter M.; Roth, J. Reece; Hong, Jae Y.; and Powers, Edward J.: Fluctuation Spectra in the NASA Lewis Bumpy-Torus Plasma, NASA TIP-1257, 1978.
6. Mallavarpu, R.; and Roth, J. R.: Investigation of Possible Lower Hybrid Emission from the NASA Lewis Bumpy Torus Plasma. NASA TM X-73689, 1977.
7. Roth, J. Reece: Optimization of Confinement in a Toroidal Plasma Subject to Strong Radial Electric Fields. NASA TM X-73690, 1977.
8. Lehnert, B.: Rotating Plasmas. Nucl. Fusion, vol. 11, 1971, pp. 485-533.
9. Tozer, B. A.: Rotating Plasma. Proc. Inst. Electr. Engr., vol. 112, Jan. 1965, pp. 218-228.
10. Hooper, E. B., Jr.: A Review of Reflex and Penning Discharges. Advances in Electronics and Electron Physics, L. Martin, ed., vol. 27, Academic Press, Inc., 1969, pp. 295-343.
11. Smirnitskaya, G. V.; and Nosyreva, I. A.: Oscillations in a Low-Pressure Penning Discharge. Sov. Phys. -Tech. Phys., vol. 15, no. 11, May 1971, pp. 1832-1838.
12. Romanyuk, L. I.; and Slobodyan, V. M.: Correlation Between the Potential and Density Fluctuations of a Plasma and the Convective Transport of Particles Across the Magnetic Field in a Penning Discharge in the Presence of Rotational Instability. NASA TT F-15026, 1973.
13. Roth, J. Reece: Experimental Study of Spectral Index, Mode Coupling, and Energy Cascading in a Turbulent, Hot-Ion Plasma. Phys. Fluids, vol. 14, no. 10, Oct. 1971, pp. 2193-2202.



14. Roth, J. Reece: Origin of Hot Ions Observed in a Modified Penning Discharge. *Phys. Fluids*, vol. 16, no. 2, Feb. 1973, pp. 231-236.
15. Roth, J. Reece: Hot Ion Production in a Modified Penning Discharge. *IEEE Trans. Plasma Sci.*, vol. PS-1, no. 1, 1973, pp. 34-45.
16. Swift, John D.; and Schwar, M. J. R.: *Electrical Probes for Plasma Diagnostics*. American Elsevier Publishing Co., Inc., 1969.
17. Reikhrudel, E. M.; Smirnitskaya, G. M.; and Ti, Nguen Khyer: Dependence of Current on Parameters in a Penning Discharge. *Sov. Phys. -Tech. Phys.*, vol. 14, no. 6, Dec. 1969, pp. 789-795.
18. Roth, J. Reece: Preliminary Scaling Laws for Plasma Current, Ion Kinetic Temperature, and Plasma Number Density in the NASA Lewis Bumpy Torus Plasma. NASA TM X-73434, 1976.
19. Roth, J. Reece; and Krawczonek, Walter M.: Paired Comparison Tests of the Relative Signal Detected by Capacitive and Floating Langmuir Probes in Turbulent Plasma from 0.2 to 10 MHz. *Rev. Sci. Instrum.*, vol. 42, no. 5, May 1971, pp. 589-594.
20. Sanmartin, Juan R.: Theory of a Probe in a Strong Magnetic Field. *Phys. Fluids*, vol. 13, no. 1, Jan. 1970, pp. 103-116.
21. Blackman, R. B.; and Tukey, J. W.: *The Measurement of Power Spectra*. Dover Publications, 1959.
22. Jenkins, Gwilyn M.; and Watts, Donald G.: *Spectral Analysis and Its Applications*. Holden-Day, Inc., 1968.
23. Smith, D. E.; Powers, E. J.; and Caldwell, G. S.: Fast-Fourier-Transform Spectral-Analysis Techniques as a Plasma Fluctuation Diagnostic Tool. *IEEE Trans. Plasma Sci.*, vol. PS-2, no. 4, Dec. 1974, pp. 261-272.
24. Kim, Young C.; and Powers, Edward J.: Effects of Frequency Averaging on Estimates of Plasma Wave Coherence Spectra. *IEEE Trans. Plasma Sci.*, vol. PS-5, no. 1, Mar. 1977, pp. 31-40.
25. Powers, Edward J.: Spectral Techniques for Experimental Investigation of Plasma Diffusion Due to Polychromatic Fluctuations. *Nucl. Fusion*, vol. 14, no. 5, Nov. 1974, pp. 749-752.
26. Roth, J. Reece: Experimental Observation of Continuity-Equation Oscillations in Slightly Ionized Deuterium, Neon, and Helium Gas. *Plasma Phys.*, vol. 11, no. 9, 1969, pp. 763-777.

1 Report No. <b>NASA TP-1258</b>		2 Government Accession No.		3 Recipient's Catalog No.	
4 Title and Subtitle <b>LOW-FREQUENCY FLUCTUATION SPECTRA AND ASSOCIATED PARTICLE TRANSPORT IN THE NASA LEWIS BUMPY-TORUS PLASMA</b>				5 Report Date <b>August 1978</b>	
				6 Performing Organization Code	
7 Author(s) <b>Chandra M. Singh, Walter M. Krawczonek, J. Reece Roth, Jae Y. Hong, Young C. Kim, and Edward J. Powers</b>				8 Performing Organization Report No. <b>E-9565</b>	
				10 Work Unit No. <b>506-25</b>	
9 Performing Organization Name and Address <b>National Aeronautics and Space Administration Lewis Research Center Cleveland, Ohio 44135</b>				11 Contract or Grant No.	
				13 Type of Report and Period Covered <b>Technical Paper</b>	
12 Sponsoring Agency Name and Address <b>National Aeronautics and Space Administration Washington, D. C. 20546</b>				14 Sponsoring Agency Code	
15 Supplementary Notes					
16 Abstract <p>The NASA Lewis bumpy-torus experiment employs a modified Penning discharge to produce and heat a plasma in a bumpy toroidal magnetic field. The strong radial electric field associated with the Penning discharge and the strong toroidal magnetic field give rise to a diversity of E/B phenomena, such as rotating waves and spokes, which in turn manifest themselves as space-time fluctuations of the plasma density and potential. The ultimate objective of the work reported herein is to further understand the nature and origin of the fluctuations and their connection with fluctuation-induced transport. The approach is to monitor the density and potential fluctuations; to digitize the data; and to generate, with the aid of a computer, various spectral properties by means of the fast Fourier transform. Of particular interest is the computer-generated transport spectrum that indicates in a quantitative way which fluctuation spectral components contribute to transport and which do not. All experimental measurements of the spectral characteristics of the plasma are given in absolute units rather than as relative values. Preliminary measurements of the transport spectrum of the ion population are given, and it is shown that the fluctuation-induced transport is in order-of-magnitude agreement with that inferred from the steady-state current flowing to the electrodes that generate the plasma.</p>					
17 Key Words (Suggested by Author(s)) <b>Plasma diffusion; Plasma transport; Plasma containment; Plasma instabilities; Plasma diagnostics; Radial diffusion; Radial transport</b>			18 Distribution Statement <b>Unclassified - unlimited STAR Category 75</b>		
19 Security Classif. (of this report) <b>Unclassified</b>		20 Security Classif. (of this page) <b>Unclassified</b>		21 No. of Pages <b>51</b>	22 Price* <b>A04</b>

\* For sale by the National Technical Information Service, Springfield, Virginia 22161

90

50